IN THE NAME OF ALLAH,
THE MOST GRACIOUS,
THE MOST MERCIFUL

Journal of Engineering and Applied Sciences (JEAS)

Vision

Pioneer journal in the publication of advanced research in engineering and applied sciences.

Mission

A peer-review process which is transparent and rigorous

Objectives

a) Support research that addresses current problems facing humanity.

b) Provide an avenue for exchange of research interests and facilitate the communication among researchers.

Scope

JEAS accepts articles in the field of engineering and applied sciences. Engineering areas covered by JEAS include:

Engineering areas

Architectural Engineering
Chemical Engineering
Civil Engineering
Computer Engineering
Electrical Engineering
Environmental Engineering
Industrial Engineering
Mechanical Engineering

Applied Sciences areas

Applied Mathematics
Applied Physics
Biological Science
Biomathematics
Biotechnology
Computer Sciences
Earth Science
Environmental Science

Correspondence and Subscription

Majmaah University, Post Box 66, Al-Majmaah 11952, KSA
email: jeas@mu.edu.sa

Journal of Engineering and Applied Sciences

Editorial

Scientific publishing has brought many challenges to authors. With increasing number of scientific journals, varying scopes and reviewing requirements, and cost of publishing to authors, finding the right journal to publish an article is a decision many authors must bitterly confront and resolve. The publication of scientific findings is an integral part of the life of researchers; and the process of publishing has evolved to become an efficient system of decimating knowledge and collaboration among scientists. Science journals have institutionalized procedures to manage large volume of article submissions per year; in many cases, journals began to define narrower scopes for a dual purpose: managing submissions and delivering outstanding research.

Based on recent studies, the scientific publishing world consists of more than 25 thousands active journals in various disciplines and fields. Science Direct hosts 3,348 journals (as of February 2014). The Directory of Open Access Journals lists in its search engine more than 9,800 open access online journals.

According to recent estimates, the number of scientific journals grows by 3% per year worldwide. With this large number of journals, journals may find it harder to stay afloat.

In its inauguration, the board of editors is honored to introduce to the scientific community the Journal of Engineering and Applied Sciences - JEAS, another scientific journal from Majmaah University. The board has pledged a commitment to JEAS authors and readers to bring the most dynamic and vibrant journal management with better satisfaction.

Dr. Tawfeeq Alkanhal

Contents

Experimental Study on Spray Characteristics of Biodiesel-Diesel Fuels Blends in a Constant Volume Chamber

Upendra Rajak

Department of Mechanical Engineering, National Institute of Technology Manipur-795004, India, upendrarajak86@gmail.com

Prerana Nashine

Manipur Technical University, Manipur, Imphal-795001, India, prerana.mech08@gmail.com
Corresponding Author

Tikendra Nath Verma

Department of Mechanical Engineering, National Institute of Technology Manipur-795004, India, verma.tikks@gmail.com

Abstract

Spray formation from diesel fuel injection through a realistic heavy-duty multi-hole injector plays a crucial role in the compression ignition engine performance. Fuel Spray characteristics influence the mixture formed in the combustion chamber which affects combustion. The present work is related to high-speed photography of fuel spray characteristics using biodiesel blends at different fuel temperatures. The spray cone angle, a time needed for full development of the spray cone, spray velocity and spray penetration were the primary study parameters. Multi-hole injectors are of paramount importance concerning the CI engines. The purpose of this work is to reveal the effects of fuel temperatures and blend effect on the spray characteristics using biodiesel and diesel fuel. Special significance was that the highest vapor fuel mass concentration was observed at the center region of the spray axis with biodiesel at a higher temperature. This is believed to be due to an increase in the number of small droplets that quickly evaporated. The mean axial velocity of droplets decreased with increasing fuel temperature. Spray penetration reduced with increasing order of fuel temperature.

Keywords: Compression ignition engine; spray characteristics; biodiesel

Introduction

The combustion process is the essential modern birthplace of energy and engine exhausts depends on consumption and combustion process of the engine. For effective combustion process, being a pre-condition for low consumption and lowered toxic greenhouse gases of the environment, it is very noteworthy to comprehend the spray formation process within the combustion, various facts of which are motionless not fully comprehend (Mar et al., 2018). The upgrade engine exhaust emission guidelines put more inflexible desires on diesel engine exhaust toxic emission performance, mainly for NO_X, particulate matter, SO_X emissions. In this regard biodiesel fuel as a new renewable clean and eco-friendly birthplace of energy was widely used due to potential capability in reducing NO_X, particulate matter, SO_X emissions (Yu et al., 2018; Rajak et al., 2018). Engine spray combustion process previous study are regularly repeated in different design parameters of engines that similar part parameter, the capability to exactly happen engine performance by existing drivers will be helpful for reducing time, cost and energy consumption in new engine upgrading (Zhou et al., 2018).

Liu et al., 2018. Investigated experiments on the macroscopic liquid phase and vapor phase spray geometry of n-heptane used of Backlit Shadowgraph and Schlieren method at different operating conditions and observed that the Mach disk position and diameter affected by injection fuel pressure and nozzle diameter. Liu et al., 2018. Investigated the cavitation phenomenon, spray morphology and primary breakup by used air or vapor bubbles with the help of a microscope and ultra-high-speed camera. Results showed that irregularly shaped bubbles due to cavitation under low pressure and prolong the bubbles with increased

Upendra Rajak et al: Experimental Study on Spray Characteristics of Biodiesel-Diesel Fuels Blends..

1

injection pressure and improved the atomization of spray at initial and end-stage with spray velocity was low surprisingly deteriorated for hot fuel. Chen et al., 2018. Studied the effect of spray incident angles on a single cylinder diesel engine performance. It was reported that the fuel consumption and soot emission decreased with increasing spray incident angle were observed at the lateral swirl combustion system and concluded that the significant effect on engine performance with maximum spray incident angle using lateral swirl combustion system.

Kobashi et al., 2019. Applied mixed fuels of diesel-ethane to a premixed charge compression ignition engine and evaluated engine characteristics. The evaluated results show that flash boiling improves the lean mixture formation and reduced soot and NOX and improved thermal efficiency of engine and ignition delay period. Balaji et al., 2014. Numerically investigated the effect of new developed spray model and model applied into KIVA4 CFD code on the diesel engine. The newly developed model ability of good captures of the spray and combustion characteristics of the engine. Shu et al. 2019. Numerically investigated the effects of spray angle on a diesel combustion characteristics. The results show that improved cylinder pressure with increasing spray angle up to 140 degrees and cylinder pressure decreased with continues to increase of spray angle. Results show a reduction in CO emission lower while higher NOX emission with increasing spray angle. Khan et al. 2018. Numerically evaluated the combined effects of spray angle and the piston bowl geometry of a direct injection diesel engine. The result showed that spray angle significant effects on engine performance and obtained to be better engine performance used of toroidal re-entrant combustion chamber geometry compared to other two geometry of toroidal combustion chamber and hemispherical combustion chamber.

Yu et al., 2018. Investigated the equilateral triangular orifice of diesel nozzle flow and spray characteristics using shadowgraph technique under different fuel injection pressure for bio-diesel and diesel fuel, their results delivered that the higher spray tip penetration and spray cone angle lower for biodiesel as compared to diesel fuel. The higher possibility of axis-switching, higher spray cone angle and spray width of diesel demonstrated superior air-fuel mixing quality than biodiesel. Das et al., 2018. Evaluated effect of spray performances with different alternative fuel (castor oil, neem oil and sunflower oil) and its blending with diesel fuel, it was observed that the mean droplet size of alternative fuel were higher and spray cone angle lower than that of petroleum base diesel fuel, due to higher viscosity and surface tension of biodiesel.

Corral- Gómez et al., 2019. Studied the effect of ternary blends of diesel-biodiesel-ethanol blends on the spray macroscopic characteristics and they found that the higher spray tip penetration due to more density and spray cone angle higher due to lower surface tension and viscosity. They concluded that the optimum blend ratio of DB30E10 is better air mixture and stable capability. Park et al., 2011. Showed the multiple-injection approaches on the spray appearances of alternative fuel. They found that the pilot injection approach characterized an advanced IMEP than the split injection approach. The multiple-injection approaches methods showed a lesser in CO, HC and soot emissions but higher NOX emission.

The present study has been carried out on the experimental investigation of an emulsion fuel involving fish oil and low sulfur diesel fuel and fuel properties, engine performance and spray characteristics with high-speed photography of fuel diesel, biodiesel, and its blends at a different fuel injection temperature. Engine tests have been performed while introducing the spray into the multi-hole injector, and data analysis was carried out to clarify the combustion engine performance.

Materials and Methods

Biodiesel production and properties:

First In this investigation, Karanja oil was used as raw material for Karanja biodiesel production for diesel engine fuel. Karanja oil was supplied from a local supplier. Transesterification method was used to convert oil to biodiesel.

The chemical reaction of the transesterification method was shown in Fig. 1 and Fig.2. In transesterification reaction, sodium hydroxide (NaOH) was used as catalyst and methanol (CH3OH) was chosen as alcohol according to previous literature (Rajak et al., 2019; Tüccar et al., 2014; Palash et al., 2015; Verma and Sharma, 2016; Kashyap et al., 2018; Singh and Verma, 2019; Rajak and Verma, 2018). The fuel properties used according to ASTM standards for density, viscosity, flash point, lower heating value, and cetane number respectively. The pure diesel and Karanja oil was obtained from the local supplier. The prepare Karanja biodiesel is mixed with pure diesel at volume basis for fifteen minutes and left thirty minutes to before used in the engine at atmospheric temperature. Blends of D100 (100% low sulphur diesel + 0% Karanja biodiesel), B20 (80% low sulphur diesel + 20% Karanja biodiesel), B40 (60% low sulphur diesel + 40% Karanja oil biodiesel), B60 (40% low sulphur diesel + 60% Karanja oil biodiesel) and B100 (0% low sulphur diesel + 100% Karanja oil biodiesel) were used at volume basis. From the previous study, the blending of 20% Karanja oil biodiesel to pure diesel has better engine performance regarding efficiency and exhaust emissions (Patel and Sankhavara, 2017). The fuels mostly tested here are blended of biodiesel and diesel fuel on a volume basis. The tested biodiesel and low sulfur diesel whose properties are illustrated in Table 1.
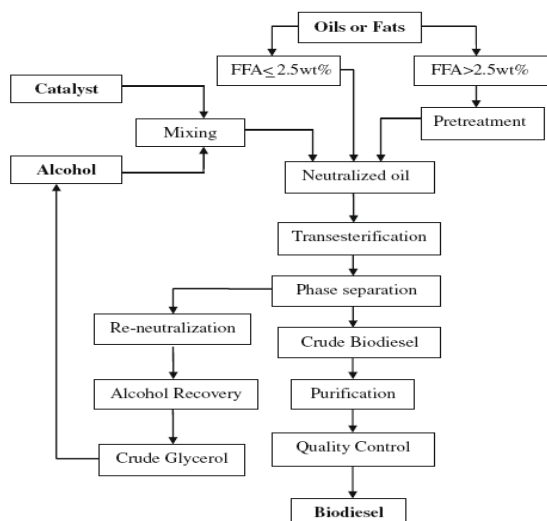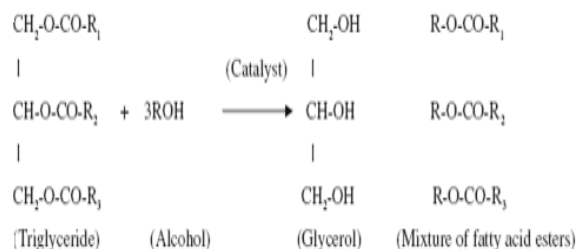

Fig.1: Biodiesel production

Fig.2: Chemical reaction [Kumar et al., 2018, Verma et al., 2017]

Table 1: Fuel properties of biodiesel and pure diesel

Fuel	Density (kg/m³)	Viscosity (mm/s²)	LHV (MJ/kg)	CN	FP (°C)
Diesel (D100)	830	3.8	42.5	48-52	76
Karanja biodiesel	877	4.4	37.5	54.0	163–187
B20	839.7	3.91	41.3	49.2	93.4
B40	849.2	4.02	40.24	50.4	110.8
B60	858.6	4.14	39.41	51.6	128.2
B80	868.1	4.27	38.5	52.8	145.6

Experiment setup: Testing was conducted in a 1-cylinder, 4-strokes, direct injection, and naturally aspirated diesel engine with a compression ratio of 17.5. The test engine and specifications of the engine are shown in Fig. 3 and Table 2. The eddy current dynamometer was connected to the engine through direct coupling for applied load. The engine load values for half and full load are measured. In order to study the effect of fuel temperature and ambient gas temperatures on the spray characteristics of biodiesel fuel, the fuel and ambient gas temperature were adjusted from 40 °C to 80 °C and at constant injection pressure of 200 bar.

The engine tests measuring with the multi-hole injector, different test conditions of 40-80 °C of fuel temperature variation were used at a constant injection pressure of 200 bar. For the spray characteristics investigation firstly the fuel is put into the fuel tank and then heated with thermocouple from constant ambient temperature condition to 40 °C and then the engine is started. When the fuel comes from the injector, pictures were taken with the help of a high-speed camera

Upendra Rajak et al: Experimental Study on Spray Characteristics of Biodiesel-Diesel Fuels Blends..

3

which is installed just in front of the injector. The reading was taken for just seconds, and with the help of this reading, analysis was performed. The multi-hole injection duration is set to 1.2 m-s. The fuel injection pressures of 200 bar are employed for sprays with the real sized injector.

Table 2: Engine specification

Description	Specification
Engine type	1-C, 4-S
Combustion system	DI
(Bore (mm) × stroke (mm	110 × 80
Compression ratio	17.5
Power	kW 3.7
Rated speed	rpm 1500
Fuel type	Diesel and biodiesel
Injector hole	Multi hole
Nozzle opening pressure	bar 200
Temperature	℃ to 80 ℃ 40
Injection strategy	1
(Start of injection (°CA b TDC	23.5

Table 3: Uncertainties within the experimental instruments

| S1. No	Instrument	Make	Type	Percentage uncertainty
1	Temperature Sensor	-	K	±0.15
2	Speed Sensor	-	PNP sensor	±1.0
3	Load indicator	-		±0.2
4	Pressure Sensor	Kistler	piezoelectric	±0.5
5	Crank Angle encoder	Kubler	pulse	±0.2
6.	Flue gas analyzer HC CO CO$_2$ NO$_X$	Testo	350 Portable	± 0.1% ± 0.3% ± 1% ± 0.5%
7	Water flow	-	Acrylic body rotameter	-
8	Burette fitted		Optical sensor	±0.5
9	Dynamometer	Power Mag	Load cell	-
10	Exhaust gas calorimeter	-	Shell and tube	-
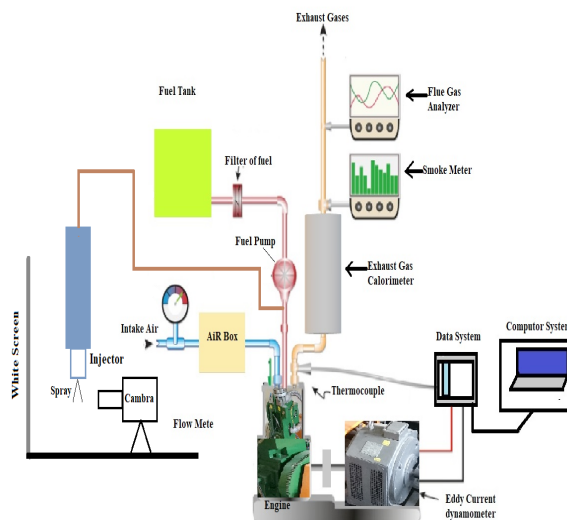
Fig. 3. Schematic diagram of the experimental setup

The uncertainty in experiment setup as shown in Table 3. The uncertainties mentioned in Table 3 is actual. Combustion characteristics of single-injection strategies only different temperatures and other parameters constant such as fuel injection pressure, injection timing, the intervals between injections, and the injection quantity ratio under diverse engine operating conditions from a compression ignition diesel engine.

Results and Discussions

Performance characteristics

Cylinder pressure: Fig. 4 demonstrates the cylinder pressure versus crank angle in the combustion chamber, for diesel, biodiesel and its blends. Fig. 4 (a) with the biodiesel blends at partial engine load and Fig. 4 (b) at full engine load. According to 4 (b) the cylinder pressure decreases with increase in blends ratio when the cylinder peak pressure is much closer to the TDC. The higher the Karanja biodiesel is, the lower cylinder peak pressure obtained. As shown in Fig. 4 (b), the cylinder peak pressure at full engine load are 79.71 bar, 77.52 bar, 75.22 bar, 73.09 bar and 72.45 bar for diesel (D100), B20, B40, B60 and for Karanja biodiesel (B100) respectively. The cylinder peak pressure decreased with increase in

percentage of Karanja oil biodiesel. With the rise of the Karanja biodiesel from 0% to 60%, the cylinder peak pressure was decreased by 8.31%.

Variation of cylinder pressure with the crank angle for diesel (D100), B20, B40, B60, and pure biodiesel (B100) fuels at partial and full loads. Consuming the D80KB20 mixture led to a close cylinder peak pressure value lower by around 2.7%. This is ascribed to the adverse effect of its higher viscosity and molecular weight which lead to inefficient use of fuel energy contents. However, the delay to obtain this peak value could be associated to the improvement in the ignition delay period important to balance the effect of the high viscosity of fuel burned that worsen the processes of fuel atomization and evaporation (Rajak and Verma, 2019; Chen et al., 2018; Elseesy et al., 2018).

Ignition delay: Ignition delay (ID) is a difference between the start of fuel injection and the start of combustion and measured regarding CA and depends on different parameters of fuel and engine. The higher cetane number of biodiesel leads to shorter ignition delay, which is responsible for lower fuel accumulation in the combustion chamber during premixed combustion phase, resulting in lower heat release rate and lower peak cylinder pressure. NOX emissions were higher while CO, smoke density and HC were reported to be lower for biodiesel compared to diesel (Rajak et al., 2018; Rajak et al., 2019; Lee et al., 2017; Salam and Verma, 2019; Rajak and Verma, 2019). The ID is one of the essential parameters for the determining engine performance. It is influenced by the physical processes and chemical processes (Elahi et al., 2018). This can be attributed to higher cetane number of biodiesel and its blends due to which ignition delay gets reduced. Ignition delay is affected by fuel spray characteristics. Fig. 5 shows variation of ignition delay versus fuel injection pressure for diesel and biodiesel.

The result shows that diesel fuel gives longer ignition delay than those of pure karanja oil biodiesel fuel (BDFP) and karanja oil biodiesel (20%) and diesel (80%) combination fuel

(BDFC), while the difference of ignition delay between BDFC and BDFP, but lower than diesel, although BDFP and BDFC give higher cetane number than that of diesel. This suggests that only the cetane number cannot provide a reasonable indication of ignition delay in all cases. With the increase of injection pressure, ignition delays of two different fuels are shortened. The enhanced fuel-air mixing rates are responsible for the decreased ignition delay. Ignition occurs at the premixed mixtures of fuel vapor and air.

Spray characteristics

Spray pictures: It can be seen in Fig. 6, spray pictures vapor phase geometry below the saturated vapor temperature of biodiesel at injection pressure of 200 bar and fuel temperature of 40 °C are shown in Fig. 7 for bottom capture.

The spray behavior of combustion performance characteristics of Karanja-diesel fuel blends at an injection pressure of 200 bar and at a different temperatures varying from 40 °C to 80 °C were analyzed using a spray visualization/analysis system and a single cylinder diesel engine. The spray visualization system consists of a fuel supply system, injector control system, visualization system, and analysis device for spray images. The fuel supply system has linked high-pressure pumps and a common-rail injection system, and a fuel filter removes fuel impurities. The injector control system has an injector driver, a digital delay/pulse generator, and a tested injector. The injection quantity of the certified injector is controlled by the opening and closing of an injector needle using a current signal.
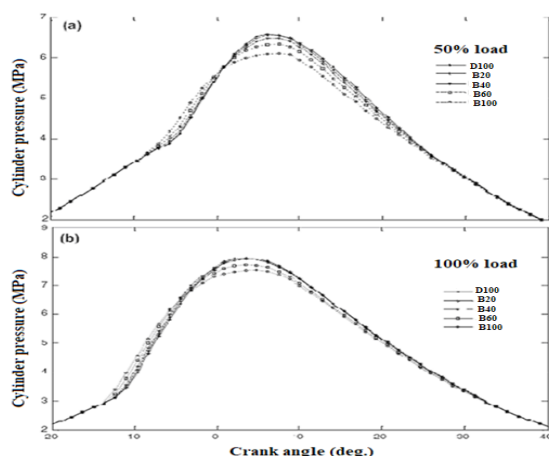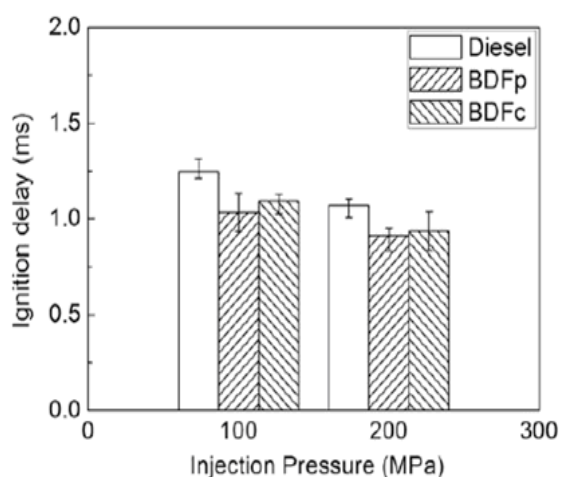
Fig. 4: Cylinder pressure with crank angle

Fig. 5: Ignition delay with fuel injection pressure

The spray images are obtained from a high-speed camera (Photron, Fastcam) with a metal-halide lamp (SA5) as a light source, a biodiesel fuel supply system, and an image acquisition-analysis device was installed. The shutter speed and frame rate of the high-speed camera were fixed to 7000 fps and 20,000 fps, respectively, and the obtained images are stored in a computer with a spray image analysis program.

Spray cone angle

Fig.8. Illustrates the variation of cone angle with diesel and its blends. It clearly shows that the maximum cone angle for diesel (D100), B20, B40, B60, B80 and biodiesel (B100) are 73.9810, 71.730, 69.20 67.470 and 67.930 respectively

at 80 °C and Similarly minimum cone angle for diesel (D100), B20, B40, B60, B80 and biodiesel (B100) are 69.040, 68.310, 67.240, 66.850, 64.850, and 64.620 at 40 °C. The reason can be attributed to the fuel temperature which when increased result in more vapor mass and lower density and viscosity. As the temperature increases cone angle increases, and it is maximum for diesel at temperature 80 °C of 73.981 degrees. The viscosity of Karanja oil is more hence which lead to decreasing the cone angle. From the figure, the biodiesel at 40 °C obtained the minimum cone angle which is 64.62 degree.

The spray cone angle described is the angle formed between two lines drawn from the nozzle tip on to the outer margins of the spray on either side of it up to some specific distance downstream of the flow. The spray cone angle of diesel was larger than that of biodiesel in all the test temperature in the present study. The higher possibility of axis-switching phenomenon, larger spray cone angle of diesel proven better air entrainment ratio and air-fuel mixing quality than biodiesel. The higher viscosity and surface tension of biodiesels increases the mean droplet size and decreases the cone angle in a fuel spray as compared to diesel. (Yu et al. and Das et al., 2018; Frijters et al., 2007; Jun et al., 2010, 41].

The cone angle is defined as the angle formed by two straight lines that stat from the exit orifice of the nozzle and tangent to the spray outline (sprays morphology) in a determined distance. The angle in a diesel spray is formed by two straight lines that are in contact with the spray's outline and at a range equivalent to 60 times de exit diameter of the orifice of the nozzle. This angle usually is between 5 and 30 degrees. This determines the fuels of macroscopic distribution in the combustion chamber greatly. In one hand, the increase in angle decreases the penetration and can cause interference between sprays (when sprays are injected using multi-orifice nozzles) in the same chamber preferring the merging of droplets. On the other hand, excessive penetration is preferred when the angle decreases lower than specific values, causing the spray to collide with the piston bowl or the combustion chamber.

Spray cone angle: Fig.8. Illustrates the variation of cone angle with diesel and its blends. It clearly shows that the maximum cone angle for diesel (D100), B20, B40, B60, B80 and biodiesel (B100) are 73.9810, 71.730, 69.20 67.470 and 67.930 respectively at 80 0C and Similarly minimum cone angle for diesel (D100), B20, B40, B60, B80 and biodiesel (B100) are 69.040, 68.310, 67.240, 66.850, 64.850, and 64.620 at 40 0C. The reason can be attributed to the fuel temperature which when increased result in more vapor mass and lower density and viscosity.
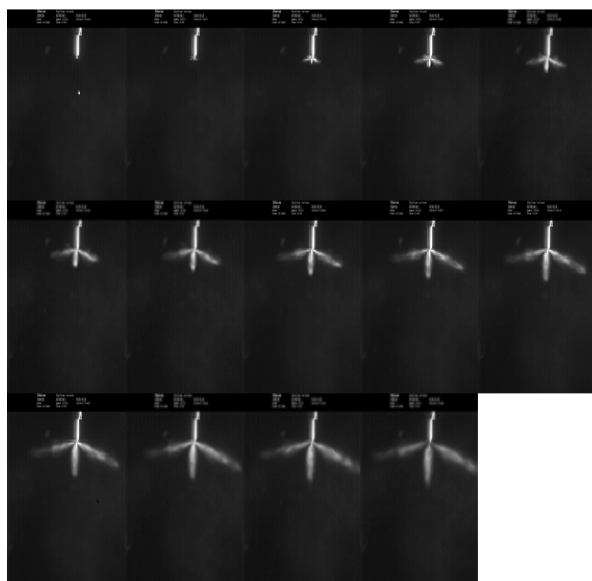

Fig. 6: Spray pictures of biodiesel at 200 bar injection pressure and 400C fuel temperature. (7000 fps) for minor plane
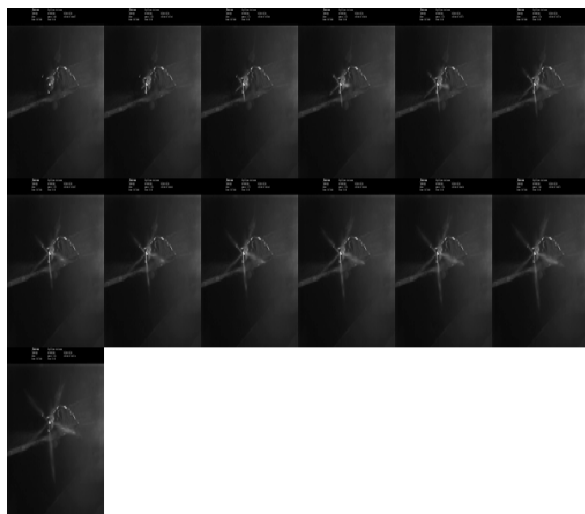

Fig. 7: Spray pictures of biodiesel at 200 bar injection pressure and 40 °C fuel temperature from bottom. (7000 fps) for major plane

As the temperature increases cone angle increases, and it is maximum for diesel at temperature 80 °C of 73.981 degrees. The viscosity of Karanja oil is more hence which lead to decreasing the cone angle. From the figure, the biodiesel at 40 °C obtained the minimum cone angle which is 64.62 degree.

The spray cone angle described is the angle formed between two lines drawn from the nozzle tip on to the outer margins of the spray on either side of it up to some specific distance downstream of the flow. The spray cone angle of diesel was larger than that of biodiesel in all the test temperature in the present study. The higher possibility of axis-switching phenomenon, larger spray cone angle of diesel proven better air entrainment ratio and air-fuel mixing quality than biodiesel. The higher viscosity and surface tension of biodiesels increases the mean droplet size and decreases the cone angle in a fuel spray as compared to diesel. (Yu et al., and Das et al., 2018; Frijters et al., 2007; Jun et al., 2010; Rajak and Verma, 2019; Chen et al., 2018).

The cone angle is defined as the angle formed by two straight lines that stat from the exit orifice of the nozzle and tangent to the spray outline (sprays morphology) in a determined distance. The angle in a diesel spray is formed by two straight lines that are in contact with the spray's outline and at a range equivalent to 60 times de exit diameter of the orifice of the nozzle. This angle usually is between 5 and 30 degrees. This determines the fuels of macroscopic distribution in the combustion chamber greatly. In one hand, the increase in angle decreases the penetration and can cause interference between sprays (when sprays are injected using multi-orifice nozzles) in the same chamber preferring the merging of droplets. On the other hand, excessive penetration is preferred when the angle decreases lower than specific values, causing the spray to collide with the piston bowl or the combustion chamber.

Upendra Rajak et al: Experimental Study on Spray Characteristics of Biodiesel-Diesel Fuels Blends..

7

Cone angle developed: Fig.9. Illustrates the variation of time taken for a fully developed spray with different fuels. The figure shows that with an increase in temperature the fuel takes more time to develop the spray cone. It clearly shows that the maximum time of cone for B20 is 0.00162 sec at 80 0C and the minimum is 0.001571sec at 40 0C. The maximum time of cone for B40 is 0.001734 sec at 80 0C, and the minimum is 0.001712 sec at 40 0C. The maximum time of cone for B60 is 0.001757 sec at 80 0C, and the minimum is 0.001714 sec.at 40 0C. The maximum time of cone for B80 is 0.001857sec at 80 0C, and the minimum is 0.001715 sec at 40 0C. The maximum time of cone for B100 is 0.001887 sec at 80 0C, and the minimum is 0.001857 sec at 40 0C. The maximum time of cone for Diesel (D100) is 0.001688 sec at 80 0C, and the minimum is 0.001571 sec at 400 ℃.

The reason can be attributed that when the temperature of biodiesel and its blends increases which results in decreasing the density and viscosity. Further due to low density and viscosity fuel takes more time to develop the spray cone. The maximum time is taken by biodiesel at a temperature of 80 °C. The reason can be attributed to the higher fuel temperature. In the experimental result, the increased fuel temperature helps in evaporation of injected droplets, which improves mixing.
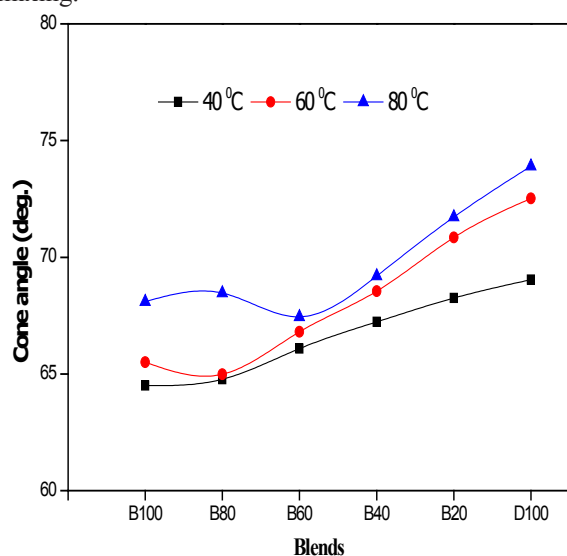

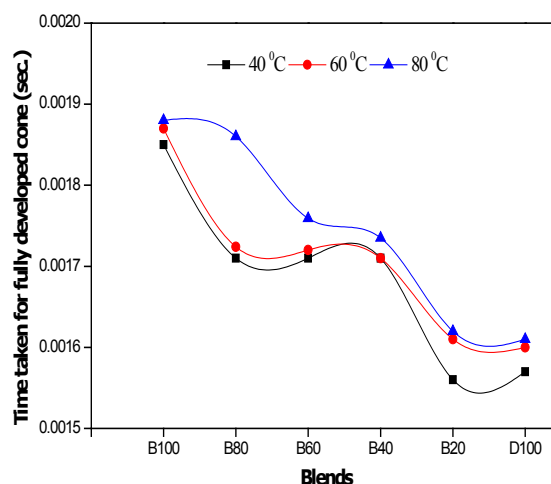Fig. 8: Effect of fuel on cone angle (degree) at different temperature

Fig. 9: Effect of fuel on time taken for fully developed cone at different temperature

Spray velocity: Fig. 10 show the effect of fuel on spray velocity as a function of temperature at engine full load. Spray velocity in the combustion chamber, it is clear from figure spray velocity is higher for biodiesel and its blends at 40 °C and lower for 80 °C as compared to regular diesel fuel. It clearly shows that the higher velocity of spray for biodiesel is 148.94 m/sec at 40 °C and lower is 134.68 m/sec at 80 °C, and the higher velocity of spray for B20 is 138.48 m/sec at 40 °C, and the lower is 130 m/sec at 80 °C. The similarly higher velocity of spray for B40 is 138.85 m/sec at 40 °C, and lower is 131.39 m/sec at 80 °C. The maximum velocity of spray for B60 is 141.91m/sec at 40 °C, and the minimum is 133.68 m/sec at 80 °C. The maximum velocity of spray for B80 is 142.27 m/sec at 40 °C, and the minimum is 138.18 m/sec at 80 °C. The higher velocity of spray was obtained for biodiesel due to higher viscosity and density of droplet, which leads to higher momentum as compared to diesel fuel. The higher chamber pressure means higher nitrogen density in the chamber that causes the greater aerodynamic force on spray, the effect of which is the shorter penetration depth. The velocity of spray has an effect on the fuel temperature and biodiesel that increases with higher viscosity and density of the fuel. The spray velocity of biodiesel were larger than that of diesel in all the temperature. Both bio-diesel

and diesel emerging from 40 °C, 60 °C and 80 °C due to higher viscosity, because the higher viscosity results in higher velocity gradient and stronger force interactions between the spray and the surrounding air (Yu, et al., 2018; Frijters et al., 2007).

Spray tip penetration: The spray tip penetration is measured by the distance travelled by the fuel from the outlet of fuel to the mixture formed within the chamber (Mar et al., 2018). Air-fuel mixing rate and air utilization are determined by fuel spray tip penetration during the combustion of the engine (Rajak et al., 2018; Chen et al., 2019, Yu et al., 2018).

Spray tip penetration depends on the fuel density, and spray tip penetration is higher with higher fuel density because of more substantial initial axial momentum from the nozzle exit. The fuel injection pressure plays a conspicuous role in spray tip penetration reported in the literature (Li et al., 2019, Khan et al., 2018).

Fig. 11, shows the variation of spray tip penetration with different fuel temperature and blend ratio of biodiesel and diesel fuel. Karanja oil-diesel and its blends under 200 bar fuel injection pressure were also compared. Spray tip penetration was obtained with similar trends when Karanja oil biodiesel added with diesel fuel at full load with constant fuel injection pressure which depicted in the figure. The decrease spray tip penetration with increasing of fuel temperature from 40 to 80 °C as abidance of figure due to higher density and viscosity of Karanja oil, which enhance the spray tip penetration and then improve the axial momentum of spray as compared to pure diesel.

It clearly shows that minimum penetration of spray is for diesel and at all temperature and maximum for biodiesel at all temperature. The maximum penetration for diesel (D100), B20, B40, B60, B80, and biodiesel (B100) is 212 mm, 234 mm, 238 mm, 242.01 mm, 244.01 and 258.1mm respectively at 40 °C and Similarly minimum penetration for diesel (D100), B20, B40, B60, B80, and biodiesel (B100) is 208 mm, 229.0022 mm, 230 mm, 231.0087 mm, 232.0086 and 244.0 mm at 80 °C The reason can be attributed to higher velocity of spray increases fuel

penetration. Three essential properties of the fuel, which effect the spray formation process, are density, viscosity and surface tension. Shows that the increase in fuel density increases spray tip penetration. This is because when the fuel density increases, the mass flow rate grow and this causes the jet momentum to increase and apply a greater force to the surrounding air, allowing it to flow easily (Das et al., 2018; Corral-gómez et al., 2019; Jun et al., 2010, Rajak and Verma, 2019).
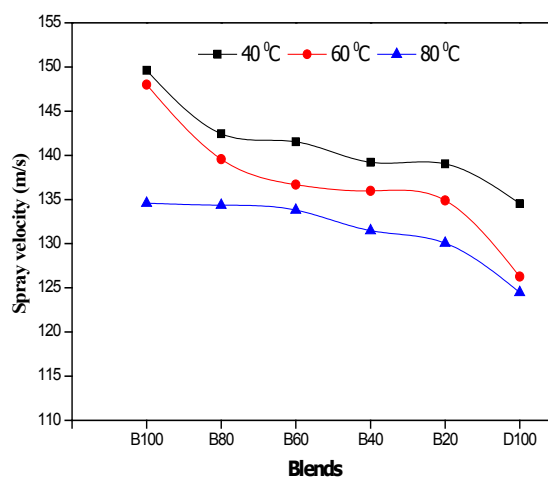

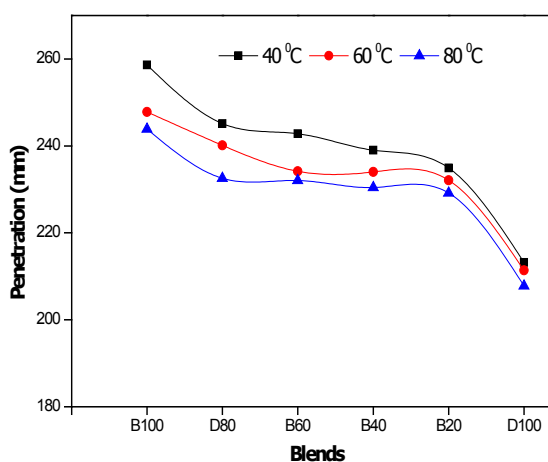Fig. 10: Effect of fuel on spray velocity at different temperature

Fig. 11: Effect of fuel on spray penetration at different temperature

Conclusion

The present investigation shows the following conclusion:

The spray cone angle of diesel was larger than that of biodiesel in all the test temperature in the present study. The higher possibility of axis-switching phenomenon, larger spray cone angle of diesel proven better air entrainment ratio and air-fuel mixing quality than biodiesel.

The effect of temperature on spray cone, spray tip penetration and velocity, cone developed and fuel injection pressure on ignition delay and cylinder pressure. Higher of fuel temperatures leads to lower tip penetration and spray velocity, and cone developed is lower.

The results revealed that the ignition delay period decreases with increase in load for all fuel used. For biodiesel the delay period was reduced by 26% when load increases from 25% to 75%. The delay period is minimum for biodiesel because of lower heating value, high density, and high viscosity.

In the analysis of the spray cone angle, it is observed that cone angle increases for each fuel with an increase in temperature and it is maximum for diesel of an angle about 73.981 degrees at 80 °C. Moreover, minimum cone angle recorded for biodiesel at 40 °C is 64.62 degree.

The analysis of the combustion characteristic of the increase in temperature fuel takes more time to form the cone. Also, it is maximum for diesel at 80 °C. Approximate increase in cone angle from 40 °C to 80 °C for diesel is 6.67%, and an increase in cone angle from 40 °C to 80 °C (fuel temperature) for biodiesel is 4.87%.

Nomenclatures

CI   Compression ignition
CN   Cetane number
DI   Direct ignition
FP   Flash point
LHV   Lower heat value
rpm   Revolution per minute
TDC   Top dead center
NOX   Nitrogen oxides
1-C   Single cylinder
4-S   Four strokes
B20   80% low sulphur diesel +20% Karanja biodiesel
B40   60% low sulphur diesel + 40% Karanja biodiesel
B60   40% low sulphur diesel + 60% Karanja biodiesel
B100   0% low sulphur diesel + 100% Karanja biodiesel
D100   100% low sulphur diesel + 0% Karanja biodiesel

Acknowledgements

References

Chen, Y., Li, X., Li, X., Zhao, W., & Liu, F., 2018. The wall-flow-guided and interferential interactions of the lateral swirl combustion system for improving the fuel/air mixing and combustion performance in DI diesel engines. Energy. 166: 690-700.

Chen, Z., He, Z., Shang, W., Duan, L., Zhou, H., Guo, G., & Guan, W., 2018. Experimental study on the effect of nozzle geometry on string cavitation in real-size optical diesel nozzles and spray characteristics. Fuel. 232: 562–571.

Chen, W., Pan, J., Liu, Y., Fan, B., Liu, H., & Otchere, P., 2019. Numerical investigation of direct injection stratified charge combustion in a natural gas-diesel rotary engine. Applied Energy. 233–234: 453–467.

Corral-gómez, L., Rubio-gómez, G., Martínez-martínez, S., & Sánchez-cruz, F. A., 2019. Effect of diesel-biodiesel-ethanol blends on the spray macroscopic parameters in a common-rail diesel injection system. Fuel.

24, 876–883.

Das, M., Sarkar, M., Datta, A., & Santra, A. K., 2018. Study on viscosity and surface tension properties of biodiesel-diesel blends and their effects on spray parameters for CI engines. Fuel. 220: 769–779.

Elahi, M., Soudagar, M., Nik-ghazali, N., Kalam, A., Badruddin, I. A., Banapurmath, N. R., & Akram, N., 2018. The effect of nano-additives in diesel-biodiesel fuel blends: A comprehensive review on stability, engine performance and emission characteristics. Energy Conversion and Management. 178: 146–177.

El-seesy, A. I., Attia, A. M. A., & El-batsh, H. M., 2018. The effect of Aluminum oxide nanoparticles addition with Jojoba methyl ester-diesel fuel blend on a diesel engine performance, combustion and emission characteristics. Fuel. 224: 147–166.

Frijters, P. J. M., Somers, L. M. T., Boer, W. A. De, & Baert, R. S. G., 2007. Macroscopic diesel fuel spray shadow graphy using high speed digital imaging in a high pressure cell. Fuel. 86: 1994–2007.

Han, S., Hyun, S., & Sik, C., 2011. Effects of multiple-injection strategies on overall spray behavior, combustion, and emissions reduction characteristics of biodiesel fuel. Applied Energy. 88(1): 88–98.

Jun, H., Han, S., & Sik, C., 2010. A study on the macroscopic spray behavior and atomization characteristics of biodiesel and dimethyl ether sprays under increased ambient pressure. Fuel Processing Technology. 91(3): 354–363.

Kashyap, S. S., Gogate, P. R., & Joshi, S. M., 2018. PT Intensified Synthesis of Biodiesel using ultrasound assisted approach. Chemical Engineering & Processing: Process Intensification. 136: 11-16.

Khan, S., Panua, R., & Kumar, P., 2018. Combined effects of piston bowl geometry and spray pattern on mixing, combustion and emissions of a diesel engine: A numerical approach. Fuel. 225: 203–217.

Kobashi, Y., Hirako, S., Matsumoto, A., & Naganuma, K., 2019. Flash boiling spray of diesel fuel mixed with ethane and its effects on premixed diesel combustion. Fuel. 237: 686–693.

Kumar, D., Singh, B., Banerjee, A., & Chatterjee, S., 2018. Cement wastes as transesterification catalysts for the production of biodiesel from Karanja oil. Journal of Cleaner Production. 183: 22-34.

Lee, S., Sik, C., Park, S., Gopal, J., Kumar, R., & Kumar, A., 2017. Spray characteristics, engine performance and emissions analysis for Karanja biodiesel and its blends. Energy. 119: 138–151.

Liu, F., Gao, Y., Zhang, Z., He, X., Wu, H., Zhang, C., & Zeng, F., 2018. Study of the spray characteristics of a diesel surrogate for diesel engines under sub / supercritical states injected into atmospheric environment. Fuel. 230: 308–318.

Liu, F., Li, Z., Wang, Z., Dai, X., He, X., & Lee, C., 2018. Microscopic study on diesel spray under cavitating conditions by injecting fuel into water. Applied Energy. 230: 1172–1181.

Li, F., Yi, B., Fu, W., Song, L., Liu, T., Hu, H., & Lin, Q., 2019. Experimental study on spray characteristics of long-chain alcohol-diesel fuels in a constant volume chamber. Journal of the Energy Institute. 9: 94-107.

Mar, S., Mar, M., Wensing, M., Vogel, T., & Praunseis, Z., 2018. A simplified model for a diesel spray. Fuel. 222: 485–495.

Mohan, B., Yang, W., & Chou, S., 2014. Development of an accurate cavitation

coupled spray model for diesel engine simulation. Energy Conversion and Management. 77: 269–277.

Palash, S. M., Masjuki, H. H., Kalam, M. A., Atabani, A. E., Fattah, I. M. R., & Sanjid, A., 2015. Biodiesel production, characterization, diesel engine performance, and emission characteristics of methyl esters from Aphanamixis polystachya oil of Bangladesh. Energy Conversion and Management. 91: 149–157.

Patel, R. L., & Sankhavara, C. D., 2017. Biodiesel production from Karanja oil and its use in diesel engine: A review. Renewable and Sustainable Energy Reviews. 71: 464-474.

Rajak, U., Nashine, P., & Verma, T. N., 2018. Comparative assessment of the emission characteristics of first, second and third generation biodiesels as fuel in a diesel engine. Journal of Thermal Engineering. Article in Press.

Rajak, U, & Verma, T. N., 2019. Influence of emission characteristic using microalgae biodiesel in diesel engine. International Research Publication House. ISBN: 978-93-87388-21-5.

Rajak, U, & Verma, T. N. (2019). Influences of engine speed variations on single cylinder direct injection diesels engine. AkiNik Publications. ISBN: 978-93-5335-124-3.

Rajak, U., & Verma, T. N., 2019. A comparative analysis of engine characteristics from various biodiesels: Numerical study. Energy Conversion and Management. 180: 904–923.

Rajak, U., Nashine, P., & Verma, T. N., 2018. Comparative assessment of the emission characteristics of first, second and third generation biodiesels as fuel in a diesel engine. Journal of Thermal Engineering. Article in Press.

Rajak, U., Nashine, P., Subhaschandra, T., & Nath, T., 2018. Numerical investigation of performance, combustion and emission characteristics of various biofuels. Energy Conversion and Management. 156: 235–252.

Rajak, U., Nashine, P., & Nath, T., 2019. Assessment of diesel engine performance using spirulina microalgae biodiesel. Energy. 166, 1025–1036.

Rajak, U., & Verma, T. N., 2018. Spirulina microalgae biodiesel - A novel renewable alternative energy source for compression ignition engine. Journal of Cleaner Production. 201: 343–357.

Rajak, U., & Verma, T. N., 2018. Effect of emission from ethylic biodiesel of edible and non-edible vegetable oil, animal fats, waste oil and alcohol in CI engine. Energy Conversion and Management. 166: 704–718.

Salam, S, & Verma, T. N., 2019. Appending empirical modelling to numerical solution for behaviour characterisation of microalgae biodiesel. Energy Conversion and Management, 180: 496-510.

Singh, T S & Verma T N., 2019. Taguchi design approach for extraction of methyl ester from waste cooking oil using synthesized CaO as heterogeneous catalyst: Response surface methodology optimization. Energy Conversion and Management, 182: 383-397.

Shu, J., Fu, J., Liu, J., Ma, Y., Wang, S., & Deng, B., 2019. Effects of injector spray angle on combustion and emissions characteristics of a natural gas (NG) -diesel dual fuel engine based on CFD coupled with reduced chemical kinetic model. Applied Energy. 233-234: 182–195.

Tuan, A., Tuan, A., & Pham, V. V., 2019. A core correlation of spray characteristics, deposit

formation, and combustion of a high-speed diesel engine fueled with jatropha oil and diesel fuel. Fuel. 244: 159–175. Tüccar, G., Tosun, E., Özgür, T., & Aydın, K., 2014. Diesel engine emissions and performance from blends of citrus sinensis biodiesel and diesel fuel. Fuel. 132: 7–11.

Verma, P., & Sharma, M. P., 2016. Comparative analysis of effect of methanol and ethanol on Karanja biodiesel production and its optimisation. Fuel: 180, 164–174.

Verma, P., Dwivedi, G., & Sharma, M. P., 2017. Comprehensive analysis on potential factors of ethanol in Karanja biodiesel production and its kinetic studies. Fuel. 188: 586–594.

Yu, S., Yin, B., Deng, W., Jia, H., Ye, Z., Xu, B., & Xu, H., 2018. Experimental study on the diesel and biodiesel spray characteristics emerging from equilateral triangular orifice under real diesel engine operation conditions. Fuel. 224: 357–365. Zhou, X., Li, T., Lai, Z., & Wang, B., 2018. Scaling fuel sprays for different size diesel engines. Fuel. 225: 358–369.

Yu, S., Yin, B., Deng, W., Jia, H., Ye, Z., Xu, B., & Xu, H. (2018). Experimental study on the spray characteristics discharging from elliptical diesel nozzle at typical diesel engine conditions. Fuel. 221: 28–34.

Yu, S., Yin, B., Deng, W., Jia, H., Ye, Z., Xu, B., & Xu, H., 2018. Experimental study on the diesel and biodiesel spray characteristics emerging from equilateral triangular orifice under real diesel engine operation conditions. Fuel. 224: 357–365.

Upendra Rajak et al: Experimental Study on Spray Characteristics of Biodiesel-Diesel Fuels Blends..

13

Numerical Investigation of 6 Chips Mounted on a Vertical Substrate in an Enclosure

Abdulmajeed Almaneea

Department of Mechanical and Industrial Engineering, College of Engineering,

Majmaah University, Majmaah 11952, Kingdom of Saudi Arabia,

a.almaneea@mu.edu.sa

Abstract

The present and future devices use from basic needs to advance lifestyle are almost governed by electronic devices which are operated by small chips. With technology advancement in controlling the temperature of electronic chips, the performance of electronic devices has been improving. Enhancing the heat dissipation from electronic chips is consequently essential in the safe and continuous operation of electronic devices. The present study investigates the methods of controlling the chip temperature for an enclosure with heat sources on both sides by varying heat sources location and Rayleigh number (Ra). Heat change is achieved by filling the gap between heat sources and cold walls with a fluid at constants Prandtl number (Pr) which converts the heat from heat sources to cold side on the top and bottom walls. Heat transfer is governed by physical mechanisms, which is lamina natural convection for the fixed enclosure. The results of the present study are validated with published work and show good agreement with previous work. The results show that with the increase of Rayleigh number (Ra), the peak temperature of the left, as well as right wall decreases and the maximum heat loss, take place when one side of heat sources on the top and the other in the bottom of the enclosure. At $R_a = 10,000$, the peak temperature along the left wall for case II and case IV is 3.7% more as compared to case I and 9.2% more as compared to case III whereas the peak temperature along the right wall for case III and case IV is 5.5% more as compared to case I and 9.2% more as compared to case II.

Keywords: Closed Enclosure, Natural Convection, Parallel Plate, Heat Transfer, Rayleigh number.

Introduction

A computer, which is widely used in the world, is a programmable machine that receives inputs, stores and manipulates data and provides output in a useful format. The computer chip or mother board has contributed significantly in the performance of computer systems. The level of the heat flux in many electronic devices which are in continuous operation has been increased by several orders of magnitude. Researchers and engineer must establish effective technology for transfer of heat from the electronic devices to an external cooling agent in order to maintain the best possible thermal environment in electronic packages. For this reason, reducing heat and dissipate it to the surrounding environment from these devices, new thermal control techniques must be capable of removing heat from hot spots within the electronic devices. Cooling of electronic equipment by natural convection is a significant thermal control mechanism in the majority of electronic appliances such as telecommunications electronics, where longtime reliability is the main factor in design criterion. For example, the heat flux in the laptop computer is expected to be of the order of 0.5 W/cm² to 480 W/cm² [1]. To maintain the components of electronic devices at or below maximum specified temperatures is the principal objective in the design criteria [2] and in most of the applications the temperature of the electronic chip should be below 85°C [3]. To avoid the existence of temperature gradient due to the fluid motion inside vertical or horizontal enclosures, isothermal boundary condition is generally adopted [4-6]. Heat Transfer due to natural convection in rectangular enclosures has many applications in engineering that widely use such as building insulation [7,8], double glazing, solar energy collectors [9,10] cooling devices for electronic instruments [11-13], nuclear reactor design [14,15] etc. Many study intensively investigate natural convection in enclosure.

Nearly 5 decade Batchelor [16] has investigated buoyancy driven flow due to the temperature difference between two side walls in rectangle geometry. Poots [17] study natural convection numerically in rectangular shape for horizontal layout and developed a numerical solution for the two-dimension governing equation. De Vahl Davis [18] and Wilkes [19] numerically investigate the natural convection in cavity with respect to cavity ratio. Some researcher has studied natural convection in different geometry such as parallel grammical, trapezoidal, triangular enclosure [20]. Yang & Nhan [21] investigated numerically the localized heat source in an enclosure for a vertical rectangular cavity with 3 heat sources on one wall whereas the opposing wall is maintained at a cold temperature. The purpose of the study is theoretical determination of the optimum spacing between the heat sources and the results shows that there is the temperature drop of 10%. Ambreen and Kim [22] studied the combined effects of three cross section (square, circular and hexagon) micro pin-fin heat sink and nanofluid using discrete phase model (DPM) by applying Constant heat flux (192 W) boundary condition at the base of heat sink in the range of $250 \leq R_e \leq 550$. The results show that circular fins have most efficient thermal performance followed by the hexagon and square fins. Hassani et al [23] numerically analyzed Water and water-based nanofluid -cooled electronic heat sink with chevron shape. Their result shows that the water-based nanofluid shows a better thermal performance and a certain penalty in the pressure drop compared to water.

Bahiraei and Heshmatian [24] evaluated the flow, heat transfer and second law characteristics of a hybrid nanofluid containing graphene–silver nanoparticles inside two new microchannel heat sinks. Their major findings are that increasing either velocity or concentration at both heat sinks, the surface temperature reduces; the cooling uniformity improves; and the maximum temperature also decreases which reduces the possibility of hot spot formation. Results also shows that the heat sink with more path changes and also using the nanofluid as heat transfer fluid can be promising options to be utilized in electronics cooling regarding both first and second laws of thermodynamics. Many researchers investigated the heat sources in enclosures under different boundary conditions [25-28].

This paper numerically investigates the effect of laminar natural convection flow and conjugate heat transfer of fixed model geometry in which on vertically placed heat sources in a sealed enclosure filled with fluid. Heat transfer enhances by increasing the temperature difference between the heat source and sink, for this aim the heat source location and Rayleigh number are variable in the present study.

Model Description

Figure 1 shows the geometry and boundary conditions of present study. Heat is generated from the heat source on left and right walls and cooled by the upper and lower walls. The conjugate heat model that combined fluid and solid approach is simulated via COMSOL. In this arangement the dimension of heat source $0.5L \times L$ which is placed on left and right walls and they are 6 heat sources. A substrate mounted on the walls with dimension $7L \times 0.25L$. The dimensions of the model are $4L \times 7L$.

S1 and S4 represents the distance between the bottom of bottom chip and the bottom wall of the enclosure; S2 and S5 represents distance between the bottom of bottom chip and the bottom of middle chip; S3 and S6 represents distance between the bottom of middle chip and the bottom of top chip. The horizontal enclosure wall perpendicular to the substrate is maintained at a constant temperature T_c, while all wall of substrate are insulated.
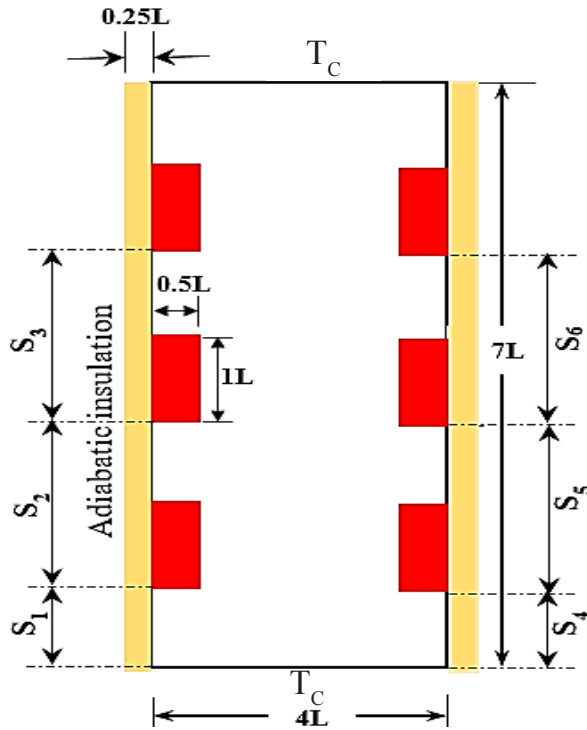
Fig. 1: The geometry of the simulation model used view the dimensions.

Fig. 2: Temperature profile along substrate surface to compare simulation model of Yang & Nhan [21] results

Table 1: Geometry arrangement in present study

	S1	S2	S3	S4	S5	S6
Case 1	0.5	2	3.5	0.5	2	3.5
Case 2	2.5	4	5.5	0.5	2	3.5
Case 3	0.5	2	3.5	2.5	4	5.5
Case 4	2.5	4	5.5	2.5	4	5.5

Investigation has been done for four cases as shown in table 1 with variation of Ra=1x103, Ra=1x105 and Ra=1x104 to make sure that the fluid behavior inside the enclosure is lamina. The simulation model is validated against results by Yang & Nhan [21], where a non-dimensional enclosure model having 3 heat sources. The buoyancy driven flow inside the enclosure is due to the temperature difference between the hot and cold walls. The validation shows a good agreement as in Fig. 2 and the average uncertainty between the simulation model presented here and the work by Yang & Nhan [21] is 2.1%.
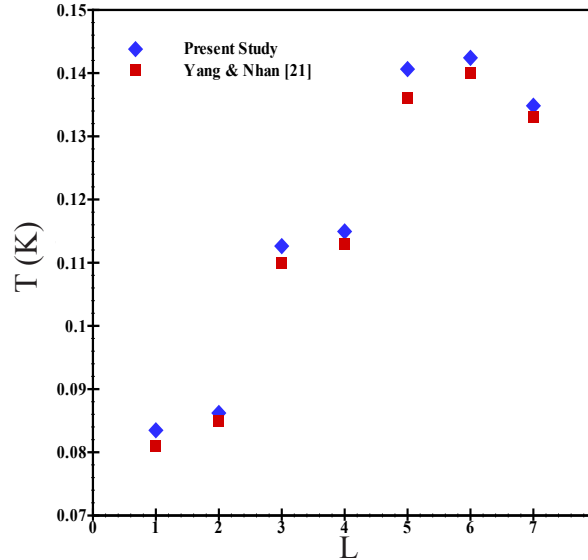
Mathematical model

In this study, the model solved as non-dimensional model. The fluid is circulating inside the enclosure due to natural convection. Before solving the full conjugate heat model, the fluid flows is checked to determine whether the flow is turbulent or laminar. For natural convection inside the enclosure, the fluid flow behaviour can be indicated by using the Rayleigh number (Ra), where Ra is 1x103, 5x103 and 1x104 to for laminar fluid. The Ra is smaller than 1x105 which indicates therefore the flow is laminar [29]. Ra is defined by specifying the heat source (Chips).

$$\left(R_a \right)$$

The applied heat generation is used to define the Rayleigh number

$$R_a = \frac{g \cdot b \cdot r^2 \cdot q_v \cdot c_p \cdot L^5}{m k_f} \qquad (1)$$

Inside the enclosure the fluid flow is laminar and governed by the non-dimensional

$$\frac{\partial u'}{\partial x'} + \frac{\partial v'}{\partial y'} = 0 \qquad (2)$$

Where:

$$x' = x/L \quad \text{and} \quad y' = y/L$$

$$u' = \frac{L}{\alpha.\sqrt{R_a.P_r}} u \quad \text{and} \quad v' = \frac{L}{\alpha.\sqrt{R_a.P_r}} v$$

$$\left(u'\frac{\partial v'}{\partial x'} + v'\frac{\partial v'}{\partial y'} \right) = -\frac{\partial p'}{\partial y'} + \sqrt{\frac{P_r}{R_a}}.\left(\frac{\partial^2 v'}{\partial x'^2} + \frac{\partial^2 v'}{\partial y'^2} \right) + F \qquad (3)$$

Where:

$$p' = \frac{\alpha^2.\rho.R_a.P_r}{L^2}.p$$

The body force is F which mainly depends on the temperature variation. This driving buoyancy force which can be expressed as:

$$F = T' \qquad (4)$$

Energy equation for the six chips

$$q_v + k_{chip}.\frac{\Delta T}{L^2}\left(\frac{\partial^2 T'^2}{\partial x'^2} + \frac{\partial^2 T'^2}{\partial y'^2} \right) = 0 \qquad (5)$$

Where

$$T' = \frac{T - T_c}{T_h - T_c} = \frac{(T - T_c).k_f}{q_v.L^2} \qquad (6)$$

The non-dimensional Energy equation for the substrate

$$\frac{k_s}{k_f}.\left(\frac{\partial^2 T'^2}{\partial x'^2} + \frac{\partial^2 T'^2}{\partial y'^2} \right) = 0 \qquad (7)$$

The boundary conditions are as follows

For all solid boundary
$$u' = 0 \qquad (8)$$

For the facing the substrate
$$F = 0 \qquad (9)$$

For adiabatic walls

$$\frac{\partial T'}{\partial n} = 0 \qquad (10)$$

The temperature continues between heat source and substrate

$$T'_{chip} = T'_s \qquad (11)$$

The heat flux continues

$$\frac{k_{chip}}{k_f}.\left(\frac{\partial T'}{\partial n} \right)_{chip} = \frac{k_s}{k_f}.\left(\frac{\partial T'}{\partial n} \right)_s \qquad (12)$$

The temperature continues between heat source and fluid

$$T'_{chip} = T'_f \qquad (13)$$

The heat flux continues

$$\frac{k_{chip}}{k_f}.\left(\frac{\partial T'}{\partial n} \right)_{chip} = \left(\frac{\partial T'}{\partial n} \right)_f \qquad (14)$$

The temperature continues between substrate and fluid

$$T'_s = T'_f \qquad (15)$$

The heat flux continues

$$\frac{k_s}{k_f}.\left(\frac{\partial T'}{\partial n} \right)_s = \left(\frac{\partial T'}{\partial n} \right)_f \qquad (16)$$

Result and Discussion

Figure 3 and fig.4 shows the temperature variation along the left and right wall respectively for Rayleigh number 1000, 5000 and 10,000 for case I. It is noted that for $0 \le L \le 2.0$ the temperature variation along the left and right wall is almost similar and temperature along the left and right wall decreases with increase of Rayleigh number. It is also noted that the temperature gradient $(\partial T/\partial L)$ is positive for $0 \le L \le 2.0$.
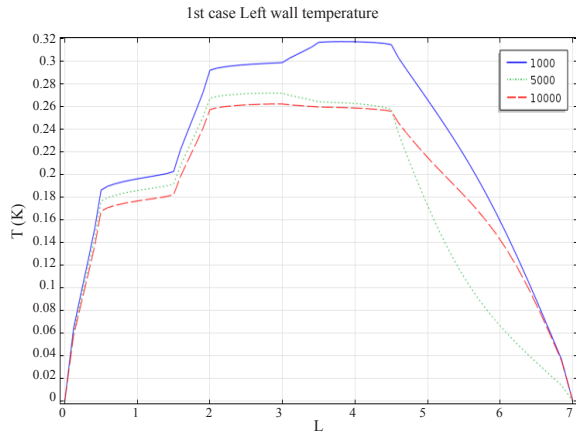
Fig. 3: Variation of temperature along the left wall for case I

For $2.0 \leq L \leq 3.0$ the temperature gradient along the left and right wall is zero as noted in fig.3 and fig.4. For $3.0 \leq L \leq 4.5$ the temperature gradient for left wall at $R_a = 10000$ is zero & for right wall at is zero. And finally for $4.5 \leq L \leq 7.0$ the temperature gradient become negative for all range of R_a. Also the temperature of left wall is higher than the temperature of right wall at $R_a = 10,000$, and the temperature of right wall is higher than the temperature of left wall at $R_a = 5000$.
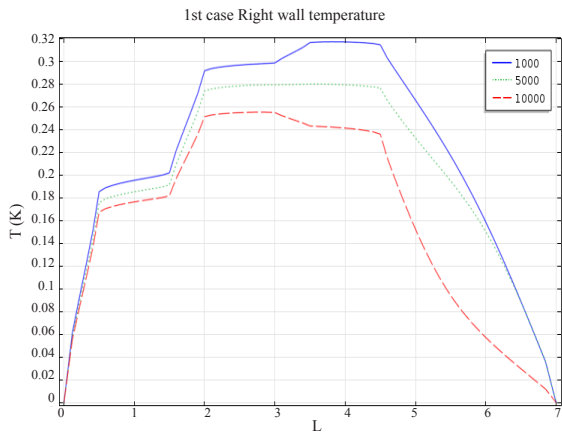

Fig. 4: Variation of temperature along the right wall for case I

Figure 5 shows the variation of surface temperature of the geometry under study at $R_a = 1000$, 5000 and 10,000 for Case I. The red colour show the least temperature whereas the white colour shows the maximum temperature. It is noted that

as the Rayleigh number increases the surface temperature in the middle portion of the geometry decreases and at $R_a = 10,000$ the variation of surface temperature is almost mirror image along the y-axis of the geometry.

Figure 6 shows the variation of velocity along the surface of the geometry under study at $R_a = 1000$, 5000 and 10,000 for Case I.
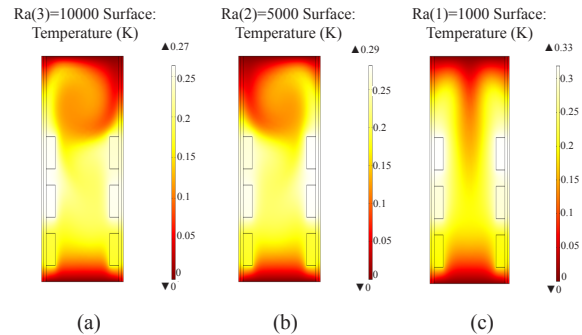

Fig. 5: Temperature profile along the surface of geometry under study for Case I at (a) Ra=1000, (b) Ra=5000 & (c) Ra=10,000

In these figures the blue colour shows the least velocity and the dark red close to black shows the maximum velocity. It is noted that the variation of velocity is minimum at the lower close to the heat sources and top most portion of the geometry and maximum at the left of upper middle portion of the geometry for value for $R_a = 1000$ and right of upper middle portion of the geometry for value for $R_a = 5000$. But at $R_a = 10,000$ the maximum velocity start shifting from the upper middle portion of the geometry to the middle portion of the geometry.
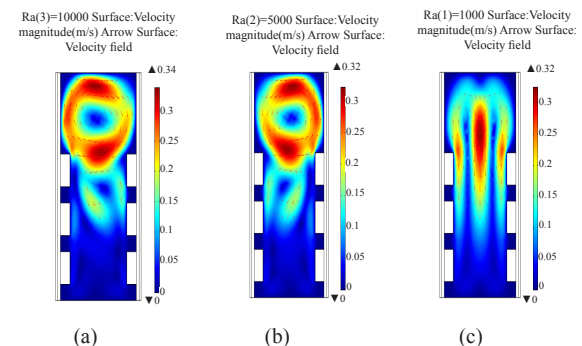

Fig. 6: velocity profile along the surface of geometry under study for Case I at (a) Ra=1000, (b) Ra=5000 & (c) Ra=10,000

Figure 7 and fig.8 shows the temperature variation along the left and right wall respectively for case II at $R_a = 1000$, 5000 and 10,000. It is noted that for both case the temperature along the wall for complete range of L increases with decrease of Rayleigh number.
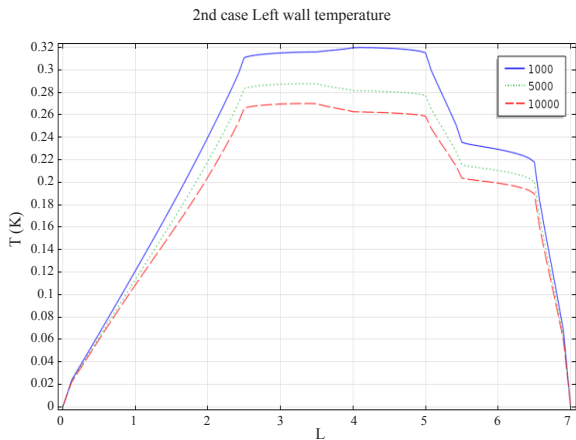

2nd case Left wall temperature

Fig. 7: Variation of temperature along the left wall for case II

It is also noted that the temperature gradient along the right wall is much more than the temperature gradient along the left wall for $0 < L \leq 0.5$ at $R_a = 1000$, 5000 and 10,000 as well as during this range the effect of Rayleigh number is negligible on wall temperature. It is also observed that the difference between the peak temperature of left and right wall at $R_a = 1000$ is very small but at $R_a = 5000$ the peak temperature of left wall 11.5% more than the peak temperature of right wall and at $R_a = 10,000$ the peak temperature of left wall 10% more than the peak temperature of right wall
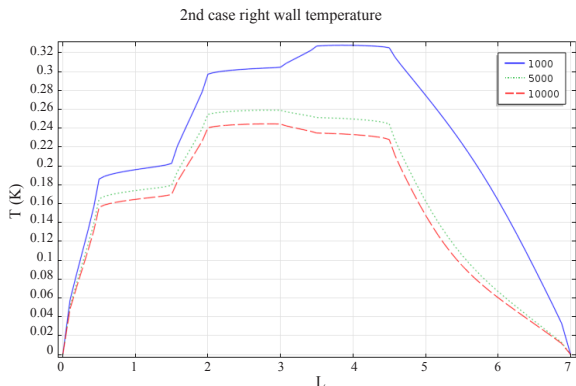

2nd case right wall temperature

Fig. 8: Variation of temperature along the right wall for case II.

Figure 9 shows the temperature profile of the surface of the geometry under study at $R_a = 1000$, 5000 and 10,000. It is noted that for $R_a = 1,000$ and $R_a = 5,000$, the surface temperature distribution is almost similar that is maximum temperature is noticed in the middle part of the geometry, but for $R_a = 10,000$, the temperature of middle part of geometry starts fall down and shifted to left upper corner and left lower corner of the geometry.

Figure 10 shows the velocity profile along the surface of the geometry under study at $R_a = 1,000$, 5000 and 10,000 for case II.

Ra(3)=10000 Surface: Temperature (K)   Ra(2)=5000 Surface: Temperature (K)   Ra(1)=1000 Surface: Temperature (K)

Fig. 9: Temperature profile along the surface of geometry under study for Case II at (a) Ra=1000, (b) Ra=5000 & (c) Ra=10,000

It is noted that the variation of velocity is minimum at the lower portion of the geometry and maximum at the right upper portion of the geometry for value for $R_a = 1000$ and $R_a = 5000$ but for $R_a = 10,000$, the velocity distribution is noticed as maximum along y-axis passing through the centre of the geometry.

Ra(3)=10000 Surface:Velocity magnitude(m/s) Arrow Surface: Velocity field   Ra(2)=5000 Surface:Velocity magnitude(m/s) Arrow Surface: Velocity field   Ra(1)=1000 Surface:Velocity magnitude(m/s) Arrow Surface: Velocity field

Fig. 10: velocity profile along the surface of geometry under study for Case II at (a) Ra=1000, (b) Ra=5000 & (c) Ra=10,000

Figure 11 and fig.12 shows the temperature variation along the left and right wall for case III at $R_a = 1000$, 5000 and 10,000. It is noted that the temperature gradient along the left is more than the temperature gradient along the right wall for $0 \leq L \leq 0.5$ but for $6.5 \leq L \leq 7.0$ the temperature gradient along the right is more than the temperature gradient along the left wall. At $R_a = 1000$ the peak temperature of both right and left wall is almost equal. For $R_a = 5000$ the peak temperature of left wall is 11.5% less than the peak temperature of right wall and for $R_a = 10,000$ the peak temperature of left wall is 15.5% less than the peak temperature of right wall.

Fig. 11: Variation of temperature along the left wall for case III

Moreover, the peak temperature of left wall at $R_a = 1000$ is almost 27% and 37.5% more than the peak temperature at $R_a = 5000$ and $R_a = 10,000$ respectively whereas the peak temperature of right wall at $R_a = 1000$ is almost 10.3% and 18.5% more than the peak temperature at $R_a = 5000$ and $R_a = 10,000$ respectively.

Fig. 12: Variation of temperature along the right wall for case III

Figure 13 shows the temperature profile along the surface of the geometry under study at $R_a = 1000$, 5000 and 10,000 for case III. It is noted that for $R_a = 1,000$ and $R_a = 5,000$, the surface temperature distribution is almost similar that is maximum temperature is noticed in the middle part of the geometry and minimum at bottom right & top left of the geometry, but for $R_a = 10,000$, the temperature of middle part of geometry start fall down.

Figure 14 shows the velocity profile along the surface of the geometry under study at $R_a = 1,000$, 5000 and 10,000 for case III. It is noted that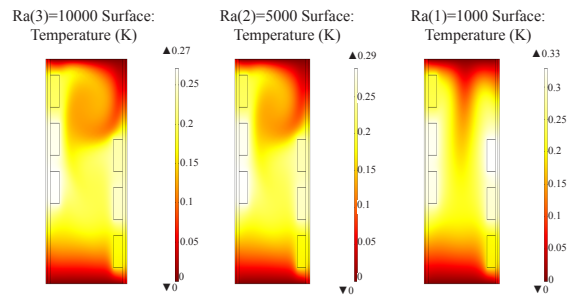 the variation of velocity is minimum at the lower portion of the geometry and maximum at the left upper portion of the geometry for value for $R_a = 1000$ and for $R_a = 5000$ but for $R_a = 10,000$, the velocity distribution is noticed as maximum along y-axis passing through the centre of the geometry.
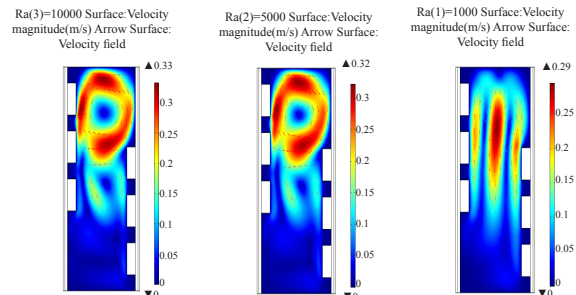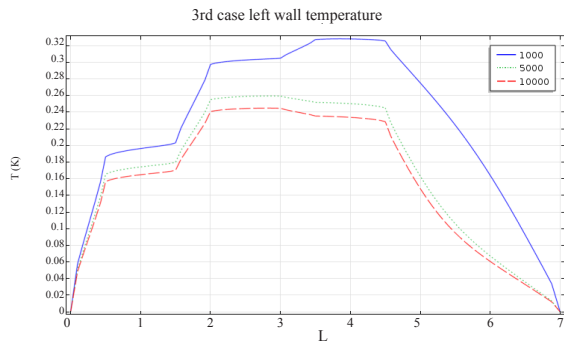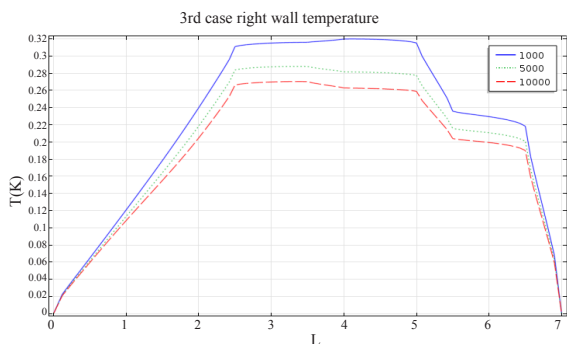

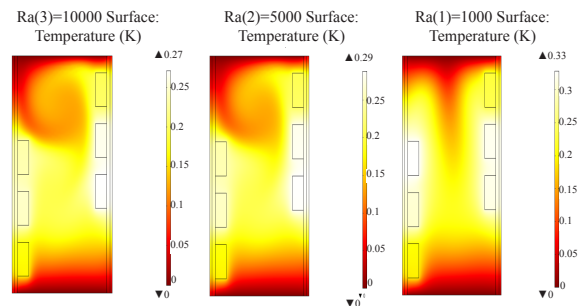Fig. 13: Temperature profile along the surface of geometry under study for Case III at (a) Ra=1000, (b) Ra=5000 & (c) Ra=10,000
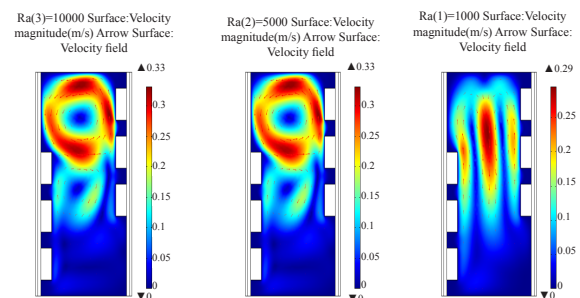

Fig. 14: velocity profile along the surface of geometry under study for Case III at (a) Ra=1000, (b) Ra=5000 & (c) Ra=10,000

Figure 15 and fig.16 shows the temperature variation along the left and right wall respectively for case IV at $R_a = 1000$, 5000 and 10,000. It is noted that temperature variation for entire range of "L" along the left and right wall is almost similar even the peak temperature at $R_a = 1000$, 5000 and 10,000 is same. It is observed that there is Sharpe increase in temperature along the left as well as right wall for $0 < L \leq 2.5$ because in this case the heat sources on both right as well as left sides of the wall are almost uniformly distributed along the entire length of wall of each sides.
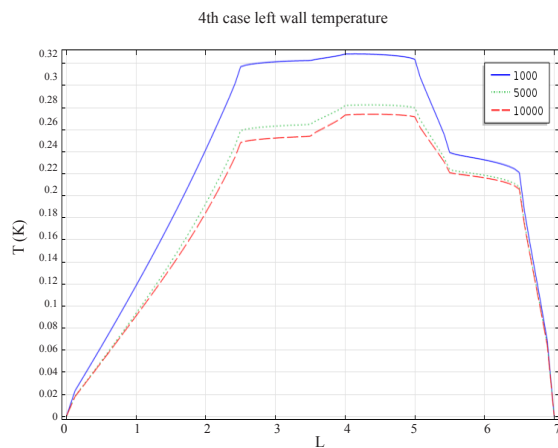
Fig. 15: Variation of temperature along the left wall for case IV
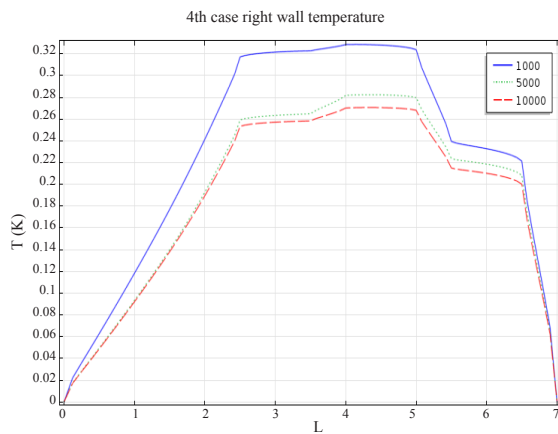
Fig. 16: Variation of temperature along the right wall for case IV

Figure 17 shows the temperature profile along the surface of the geometry under study at $R_a = 1,000$, 5000 and 10,000 for case IV. It is noted that as the Rayleigh number increases the surface temperature distribution is more uniform in the middle portion of the geometry at lower value of Rayleigh number and at $R_a = 10,000$ the variation of surface temperature is almost mirror image along the y-axis of the geometry.
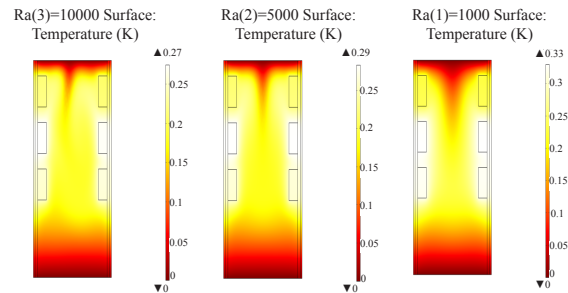
Fig. 17: Temperature profile along the surface of geometry under study for Case IV at (a) Ra=1000, (b) Ra=5000 & (c) Ra=10,00
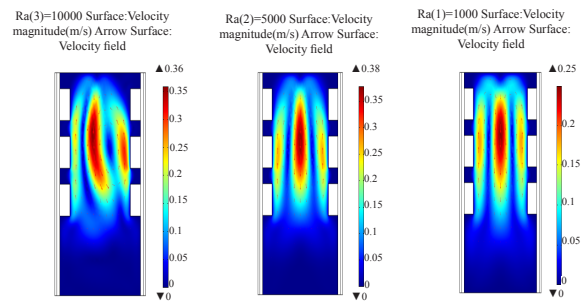
Fig. 18: velocity profile along the surface of geometry under study for Case IV at (a) Ra=1000, (b) Ra=5000 & (c) Ra=10,000

Figure 18 shows velocity profile along the surface of the geometry under study at $R_a = 1,000$, 5000 and 10,000 for case IV. It is noted that the variation of velocity is minimum at the lower portion of the geometry and maximum at the upper middle portion of the geometry.

Conclusions

The present study is the numerical study using

COMSOL software for the geometry shown in Figure 1 in which heat is generated from the heat source on left and right walls and cooled by the upper and lower walls. Based on the analysis as discussed in section 4 the following conclusion have been drawn from this study

As the Rayleigh number increases the peak temperature on the both sides of the wall of the geometry under study decreases for all four cases.

In general, as the Rayleigh number the temperature distribution along the surface of the geometry become more uniform.

The velocity distribution is more in the upper half of the geometry.

The peak temperature along the left wall at $R_a = 10,000$ is maximum for case II and case IV which 3.7% more as compared to case I and 9.2% more as compared to case III.

The peak temperature along the right wall at $R_a = 10,000$ is maximum for case III and case IV which 5.5% more as compared to case I and 9.2% more as compared to case II.

Nomenclatures	
R_a	Rayleigh number
P_r	Prandtl number
L	Length of clip wall
b	Thermal Expansion Coefficient
a	Thermal Diffusivity
r	Density
c_p	Specific Heat Capacity
k	Thermal Conductivity
m	Dynamic Viscosity
q_v	Heat Generation
T	Temperature
p	Pressure

F	Body force
u	Velocity in x-direction
v	Velocity in y-direction
n	Normal
Subscripts	
f	Fluid
s	Substrate
$chip$	Chip
c	Cold

References

Mohamed H.A. Elnaggar, Ezzaldeen Edwan, "Heat Pipes for Computer Cooling Applications", Electronics Cooling, Chapter 4, 2016.

Peterson, G. P., and Ortega, A., "Thermal control of electronic equipment and devices," In Advances in Heat Transfer, 1990 (20); pp. 181-314.

Ramaswamy, C., Joshi, Y., Nakayama, W., and Johnson, W., "High speed visualization of boiling from an enhanced structure," Int. J. Heat and Mass Transfer, 2002(45); pp. 4761- 4771.

Hasnaoui, M., Bilgen, E., and Vasseur, P., "Natural convection heat transfer in rectangular cavities heated from below," J. Thermo-physical Heat Transfer, 1992(6); pp. 255-264.

Valencia, A., and Frederick, R., "Heat Transfer in square cavities with partially active vertical walls," Int. J. Heat and Mass Transfer, 1989(32); pp. 1567-1574.

Selamet, E., Arpaci, V. S., and Borgnakke, C., "Simulation of laminar buoyancy driven flows in an enclosure," Numerical Heat Transfer, 1992 (22); pp. 401-420.

Miroshnichenko IV, Sheremet MA, Mohamad AA. "Numerical simulation of a conjugate turbulent natural convection combined with surface thermal radiation in an enclosure with a heat source", Int. J Therm. Sci., 2016(109); pp.172–181.

Sheremet MA, Miroshnichenko IV. "Numerical study of turbulent natural convection in a cube having finite thickness heat-conducting walls", Heat Mass Transf., 2015(51); pp.1559–1569.

Lakeh RB, Lavine AS, Kavehpour HP, Wirz RE, "Study of turbulent natural convection in vertical storage tubes for supercritical thermal energy storage", Numerical Heat Transf., 2015(67); pp.119–139.

Muresan C, Menezo C, Bennacer R, Vaillon R. "Numerical simulation of a vertical solar collector integrated in a building frame: radiation and turbulent natural convection coupling", Heat Transf. Eng., 2006(27); pp.29–42.

Baudoin A, Saury D, Bostrom C., "Optimized distribution of a large number of power electronics components cooled by conjugate turbulent natural convection", Applied Thermal Engineering, 2017(124); pp.975–985.

Vasco DA, Zambra C, Moraga NO., "Numerical simulation of conjugate forced turbulent heat convection with induced natural laminar convection in a 2D inner cavity", Int. J. Therm. Sci., 2015(87); pp.121–135.

Bessaih R, Kadja M., "Turbulent natural convection cooling of electronic components mounted on a vertical channel", Appl. Therm. Eng., 2000(20); pp.141–54.

Swartz MM, Yao S., "Experimental study of turbulent natural-convective condensation on a vertical wall with smooth and wavy film interface", Int. J. Heat Mass Transf. 2017(113); pp.943–60.

Anderson MH, Herranz LE, Corradini ML., "Experimental analysis of heat transfer within the AP600 containment under postulated accident conditions", Nuclear Eng. Des. 1998(185); pp.153–72.

Batchelor GK., "Heat transfer by free convection across a closed cavity between vertical boundaries at different temperatures", J. Appl. Math, 1954(12); pp.209–33.

Poots G., "Heat transfer by laminar free convection in enclosed plane gas layers", Q J Mech. Appl. Math, 1958(11); pp.257–73.

De Vahl Davis G., "Laminar natural convection in an enclosed rectangular cavity", Int. J. Heat Mass Transf. 1968(11); pp.1675–93.

Wilkes JO, Churchill SW., "The finite difference computation of natural convection in a rectangular enclosure", Am. Inst. Chem. Eng. 1966(12(1)); pp.161–166.

Das D, Roy M, Basak T., "Studies on natural convection within enclosures of various (non-square) shapes – a review", Int. J. Heat Mass Transf., 2017(106); pp.356–406.

Phan-Thien, Y.L. Nhan, "An optimum spacing problem for three chips mounted on a vertical substrate in an enclosure", Numerical Heat Transfer: Part A: Applications, 2000(37(6)); pp. 613-630.

Ambreen T, Kim Man-Hoe, "Effect of fin shape on the thermal performance of nanofluid-cooled micro pin-fin heat sinks", International Journal of Heat and Mass Transfer 2018(126); pp. 245–256.

Hassani .S.M, Khoshvaght-Aliabadi .M, Mazloumi S.H, "Influence of chevron fin interruption

on thermo-fluidic transport characteristics of nanofluid-cooled electronic heat sink", Chemical Engineering Science 2018 (191); pp.436–447.

Bahiraei .M, Heshmatian. S, "Thermal performance and second law characteristics of two new microchannel heat sinks operated with hybrid nanofluid containing graphene–silver nanoparticles", Energy Conversion and Management, 2018(168); pp. 357–370.

Bahiraei .M, Heshmatian. S, "Electronics cooling with nanofluids: A critical review", Energy Conversion and Management, 2018(172); pp. 438–456.

Heindel, T., S. Ramadhyani, F. Incropa, "Conjugate natural convection from an array of protruding heat sources", Numerical Heat Transfer, Part A Applications, 1996(29(1)); pp. 1-18.

Keyhani, M., L. Chen, D. Pitts, "The aspect ratio effect on natural convection in an enclosure with protruding heat sources", Journal of Heat Transfer (Transaction of ASME, Series), USA, 1991(113(4))

Wroblewski, D., Y. Joshi, "Liquid immersed cooling of a substrate mounted protrusion in three dimensional enclouser: the effect of geometry and boundary condition", Journal of heat transfer, 1994(116(1)); pp. 112-119.

MacGregor, R., "Free convection through vertical plane layers-moderate and high Prandtl number fluids", Trans. ASME, Journal of Heat Transfer, 1969(91); pp. 391-403.

λ-Generalized Gamma Functions

Asifa Tassaddiq

College of Computer and Information Sciences Majmaah University, Al Majmaah 11952,
Saudi Arabia
a.tassaddiq@mu.edu.sa

Abstract

The objective of present research is to introduce and analyze a new special function that occurs as a part of the kernel of the integral representation of the λ-generalized Hurwitz-Lerch zeta functions. One important aspect of the analysis of special functions is to study their properties. It is found that λ-generalized gamma function satisfies the log convex and derivative properties. Recurrence relation and reflection formula are achieved that are always important to study the behavior of new functions. As an application, a new series representation of the λ-generalized Hurwitz-Lerch zeta functions is established. These new results are validated by analyzing their important cases that agree with the known results. It is interesting to note that the coefficients in the series representation of the family of zeta functions are generalized from "1" to "gamma function" and then to "generalized gamma" and "λ-generalized gamma functions" in a simple and natural way.

Keywords: λ-generalized Hurwitz-Lerch zeta function; analytic number theory; λ-generalized gamma functions; derivative properties; series representation

Introduction

1.1. Preliminaries and Nomenclature

An extension of gamma function was introduced and defined by Chaudhry and Zubair [1] as

$$\Gamma_b(s) = \int_0^\infty t^{s-1} e^{-t-\frac{b}{t}} dt,$$
$$(b > 0; b = 0, s = \sigma + i\tau; \sigma = \Re(s) > 0) \quad (1)$$

It extends the integral representation of the original gamma function from $\Re(s) > 0$ to all s by inserting the factor $e^{-\frac{b}{t}}$. When b=0, it reduces to the original gamma function

$$\Gamma(s) = \int_0^\infty t^{s-1} e^{-t} dt, \qquad (\Re(s) > 0) \quad (2)$$

Many interesting properties and important applications of the generalized gamma functions have been discussed in the literature. For example, it appears as a solution of boundary value problems in heat conduction problems due to laser source [1]. The derivative of gamma function is called digamma function is defined as [1,p.20]

$$\psi(s) = \frac{d}{ds}\left(\ln(\Gamma(s))\right) = \frac{\frac{d}{ds}(\Gamma(s))}{\Gamma(s)} \quad (3)$$

Lately, Srivastava discussed and analysed an innovative family of Hurwitz-Lerch zeta functions defined by [2, p. 1487, Equation (1.14)]

$$\Phi_{\lambda_1,\ldots,\lambda_p,\mu_1,\ldots,\mu_q}^{(\rho_1,\ldots,\rho_p,\sigma_1,\ldots,\sigma_q)}(z, s, a; b, \lambda) :=$$

$$\frac{1}{\Gamma(s)} \int_0^\infty t^{s-1} \exp\left(-at - \frac{b}{t^\lambda}\right) {}_p\Psi_q^* \left[\begin{matrix} (\lambda_1, \rho_1), \ldots, & (\lambda_p, \rho_p) \\ (\mu_1, \sigma_1), \ldots, & (\mu_p, \sigma_p) \end{matrix} ; ze^{-t} \right] dt$$

$$\left((\lambda \geqq 0; \Re(b) \geqq 0; \min[\Re(s), \Re(a)] > 0) \right) \quad (4)$$

In this case, we can get the relation with extended Hurwitz-Lerch zeta functions $\Phi_{\lambda_1,\ldots,\lambda_p,\mu_1,\ldots,\mu_q}^{(\rho_1,\ldots,\rho_p,\sigma_1,\ldots,\sigma_q)}(z, s, a)$ defined by [3, p. 503, Equation (6.2)] (see also [4] and [5])

$$\Phi_{\lambda_1,\ldots,\lambda_p,\mu_1,\ldots,\mu_q}^{(\rho_1,\ldots,\rho_p,\sigma_1,\ldots,\sigma_q)}(z, s, a; 0, \lambda) = \Phi_{\lambda_1,\ldots,\lambda_p,\mu_1,\ldots,\mu_q}^{(\rho_1,\ldots,\rho_p,\sigma_1,\ldots,\sigma_q)}(z, s, a)$$

$$= e^b \Phi_{\lambda_1,\ldots,\lambda_p,\mu_1,\ldots,\mu_q}^{(\rho_1,\ldots,\rho_p,\sigma_1,\ldots,\sigma_q)}(z, s, a; b, 0) \quad (5)$$

In the above equation (4), ${}_p\Psi^*q$ where (p, $q \in N_0 = \{0,1,2,..\}$) is the usual Fox-Wright function given by [5, p. 2219, Equation 1] (see also [4, p. 516, Eq. (1)] and [3, p. 493, Eq. (2.1)]

$$_p\Psi^*q \left[\begin{matrix} (\lambda_1, \rho_1), \ldots, & (\lambda_p, \rho_p) \\ (\mu_1, \sigma_1), \ldots, & (\mu_q, \sigma_q) \end{matrix} ; z \right] = \sum_{\chi=0}^\infty \frac{([\lambda_p])_{\rho_p\chi}}{([\mu_q])_{\sigma_q\chi}} \frac{z^\chi}{\chi!} . (6)$$

Pochammer symbols $\left([\lambda_p]\right)_{\rho_p n} := [\lambda_1]_{\rho_p n} \cdots$ $[\lambda_p]_{\rho_p n}$ indicate the shifted factorial that can be

written in terms of the basic gamma functions as also defined in [6] are given here

$$(\lambda)_\rho = \frac{\Gamma(\lambda + \rho)}{\Gamma(\lambda)}$$
$$= \begin{cases} 1 & (\rho = 0, \rho \in \mathbb{C} \setminus \{0\}) \\ \lambda(\lambda + 1) \dots (\lambda + \chi - 1) & (\rho = \chi \in \mathbb{N}; \lambda \in \mathbb{C}), \end{cases} \quad (7)$$

$$\Delta := \sum_{j=1}^{q} \sigma_j - \sum_{j=1}^{p} \rho_j \text{ and } \nabla := \left(\prod_{j=1}^{p} \rho_j^{-\rho_j}\right) \cdot \left(\prod_{j=1}^{q} \sigma_j^{\sigma_j}\right).$$

The series representation as given by (6) is well defined in the entire complex *z*-plane for $\Delta > -1$; and if $\Delta = 0$, the series (6) is meaningful only for $|z| < \nabla$. The concerned reader is mentioned to see also the references [7-9] for further study of Fox-Wright and related functions.

λ-generalized Hurwitz-Lerch zeta functions and its diverse formulae have attracted a notable apprehension and several research articles have been emerged about these functions. Luo and Raina [10], and Jankov et al. [11] have established some inequalities involving λ-generalized Hurwitz-Lerch zeta functions. The inclusion properties of definite subclass of special type of meromorphic functions have been investigated by Srivastava et al. [12]. Some new expansion formulae are considered by Srivastava and Gaboury [13] comprising of these functions, (see, for details, [14] and [15]. An expository article [16] by Srivastava presents significant identities involving the zeta and related functions. Choi et al. [17] have generalized these functions by making use of one additional variable. An interesting integral transform associated with the λ-extended Hurwitz–Lerch zeta function is presented by Srivastava et al. [18]. More recently, Tassaddiq [19] has established a new representation for this family of the **λ**-generalized Hurwitz-Lerch zeta functions in the form of complex delta functions such that these functions are defined over the space of entire functions. The significant special cases of Srivastava's λ-generalized Hurwitz-Lerch zeta functions are enumerated in the form of a table [19, p.4]. To accomplish the idea of this paper, we present this table on the next page. For more clarity, this table can be generated from equation (4) by taking into account of its certain special cases. The readers interested in further exhaustive analysis of zeta and related functions are mentioned to bibliography [20–43].

1.2 Motivation and Objectives

Hurwitz-Lerch zeta functions have always been remained of significant importance for numerous researchers due to its influence in analytic number theory and other applied sciences. The Riemann hypothesis is a well-known unsolved problem in analytic number theory [23]. It states that "all the non-trivial zeros of the zeta function exist on the real line s=1/2". These zeros seem to be complex conjugates and hence symmetric on this line. Hurwitz-Lerch zeta functions and its generalizations are vital in the study of Riemann hypothesis and for the investigation of zeta functions themselves. The study of distributions in statistical inference and reliability theory [2, 43-44] also involves these functions. By taking inspiration of all the above discussion, the objective of present research is to introduce and analyze a new special function that occurs as a part of the kernel of the integral representation of the λ-generalized Hurwitz-Lerch zeta functions. It appears to be a natural generalization of gamma function and therefore it is named here as λ-generalized gamma function. One important aspect of the analysis of special functions is to study their properties. It is found that λ-generalized gamma function satisfies the log convex and derivative properties. A recurrence relation and a reflection formula are obtained that are always important to study the behavior of new functions. As an application, a new series representation of the λ-generalized Hurwitz-Lerch zeta functions is obtained. These new results are validated by analyzing their important cases that agree with the known results. It is interesting to note that the coefficients in the series representation of the family of zeta functions are generalized from "1" to "gamma function" and then to "generalized gamma" and "λ-generalized gamma functions" in a simple and natural way.

The organization of the paper is given as: The λ-generalized gamma function is introduced and defined in Section 2 by discussing some properties of these functions. Similar outcomes are achieved for gamma functions. As an application, a new series representation of Srivastava's λ-generalized Hurwitz-Lerch zeta functions is obtained. Some known special cases are verified in order to validate these new results achieved by using the λ-generalized gamma functions. This analysis is summarized in the last Section 3. Throughout this investigation, conditions on the parameters will be considered standard as given in (1)-(7) unless otherwise stated.

Table 1. Different Special Cases of λ-Generalized Hurwitz-Lerch Zeta Functions. [19]

Functions	$\min[\Re(\alpha),\Re(s)]>0;\ \Re(b)\ge 0;\ \lambda\ge 0;$ $\rho=\rho_1,\dots,\rho_p,\ \sigma=\sigma_1,\dots,\sigma_q;\ \lambda^*=\lambda_1,\dots,\lambda_p;\ \mu=\mu_1,\dots,\mu_q$	(p−1 = q = 0; λ₁ = μ; ρ₁ =1)				b = 0	(p−1 = q = 0; λ₁ = μ; ρ₁ =1)	
			λ = 1	μ = 1	λ = μ = 1		b = 0	μ = 1; b = 0
λ-Generalized Hurwitz-Lerch Zeta Functions $\Phi^{(\rho;\sigma)}_{\lambda^*,\mu}(\pm e^{-x},s,a;b,\lambda)$	$\Phi^{(\rho;\sigma)}_{\lambda^*,\mu}(\pm z,s,a;b,\lambda)$ [2]	$\Phi^{\lambda}_{\mu}(\mp z,s,a;b)$ [45-46]	$\Phi^{*}_{\mu}(\pm z,s,a,b)$	$\Phi_b(\pm z,s,a,\lambda)$	$\Phi_b(\pm z,s,a)$	$\Phi^{(\rho;\sigma)}_{\lambda^*,\mu}(\pm z,s,a,b)$ [2-3]	$\Phi^{*}_{\mu}(\pm z,s,a)$ [46]	$\Phi(\pm z,s,a)$ [47]
λ-Generalized Extended Fermi-Dirac and Extended Bose-Einstein Functions $\Phi^{(\rho;\sigma)}_{\lambda^*,\mu}(\pm e^{-x},s,a+1;b,\lambda)$	$\Theta^{(\rho;\sigma)}_{\lambda^*,\mu}(x,s,a;b,\lambda)$	$\Theta^{\lambda}_{\mu}(x,s,a;b)$	$\Theta^{*}_{\mu}(x,s,a,b)$	$\Theta_b(x,s,a;\alpha;\lambda)$	$\Theta_b(x,s,a,\lambda)$, $\Theta_b(x,s,a)$	$\Theta^{(\rho;\sigma)}_{\lambda^*,\mu}(x,s,a)$	$\Theta^{*}_{\mu}(x,s,a)$ [48]	$\Theta_a(x;s)$ [49]
	$\Psi^{(\rho;\sigma)}_{\lambda^*,\mu}(x,s,a;b,\lambda)$	$\Psi^{\lambda}_{\mu}(x,s,a;b)$	$\Psi^{*}_{\mu}(x,s,a,b)$	$\Psi_b(x,s,a,\lambda)$	$\Psi_b(x,s,a)$	$\Psi^{(\rho;\sigma)}_{\lambda^*,\mu}(x,s,a)$	$\Psi^{*}_{\mu}(x,s,a)$ [48]	$\Psi_a(x;s)$ [49]
λ-Generalized Polylogarithm Functions $\Phi^{(\rho;\sigma)}_{\lambda^*,\mu}(\pm z,s,1;b,\lambda)$	$\mathrm{Li}^{(\rho;\sigma)}_{\lambda^*,\mu}(\pm z,s;b,\lambda)$	$\mathrm{Li}^{\lambda}_{\mu}(\mp z,s,a;b)$	$\mathrm{Li}^{*}_{\mu}(z,s,b)$	$\mathrm{Li}_b(z,s,\lambda)$	$\mathrm{Li}_b(z,s)$	$\mathrm{Li}^{(\rho;\sigma)}_{\lambda^*,\mu}(z,s)$	$\mathrm{Li}^{*}_{\mu}(z,s)$ [48]	$\mathrm{Li}_s(z)$ [47]
λ-Generalized Fermi-Dirac and Bose Einstein Functions	$F^{(\rho;\sigma)}_{\lambda^*,\mu}(x,s;b,\lambda)$	$F^{\lambda}_{\mu}(x,s,a;b)$	$F^{*}_{\mu}(x,s,b)$	$F_b(x,s,\lambda)$	$F_b(x,s)$	$F^{(\rho;\sigma)}_{\lambda^*,\mu}(x,s)$	$F^{*}_{\mu}(x,s)$ [48]	$F_s(x)$ [49]
	$B^{(\rho;\sigma)}_{\lambda^*,\mu}(x,s;b,\lambda)$	$B^{\lambda}_{\mu}(x,s,a;b)$	$B^{*}_{\mu}(x,s,b)$	$B_b(x,s,\lambda)$	$B_b(x,s)$	$B^{(\rho;\sigma)}_{\lambda^*,\mu}(x,s)$	$B^{*}_{\mu}(x,s)$ [48]	$B_s(x)$ [49]
λ-Generalized Hurwitz zeta Functions $\Phi^{(\rho;\sigma)}_{\lambda^*,\mu}(\pm 1,s,a;b,\lambda)$	$\zeta^{(\rho;\sigma)}_{\lambda^*,\mu}(s,a;b,\lambda)$	$\zeta^{\lambda}_{\mu}(s,a;b)$	$\zeta^{*}_{\mu}(s,a,b)$	$\zeta_b(s,a,\lambda)$	$\zeta_b(s,a)$ [1]	$\zeta^{(\rho;\sigma)}_{\lambda^*,\mu}(s,a)$	$\zeta^{*}_{\mu}(s,a)$ [48]	$\zeta(s,a)$ [47]
λ-Generalized Riemann Zeta Functions $\Phi^{(\rho;\sigma)}_{\lambda^*,\mu}(\pm 1,s,1;b,\lambda)$	$\zeta^{(\rho;\sigma)}_{\lambda^*,\mu}(s)$	$\zeta^{\lambda}_{\mu}(s;b)$	$\zeta^{*}_{\mu}(s,b)$	$\zeta_b(s,\lambda)$	$\zeta_b(s)$ [1]	$\zeta^{(\rho;\sigma)}_{\lambda^*,\mu}(s)$	$\zeta^{*}_{\mu}(s)$ [48]	$\zeta(s)$ [47]

Results

2.1. Definition and properties of the λ-generalized gamma functions

In this section, a new special function namely λ-generalized gamma function is introduced and defined as follows

$$\Gamma_b^\lambda(s;a) = \int_0^\infty t^{s-1} \exp\left(-at - \frac{b}{t^\lambda}\right) dt$$
$$(\lambda \geqq 0; \Re(b) \geqq 0; \min[\Re(s), \Re(a)] > 0). \quad (8)$$

By substituting $a = \lambda = 1$ in the above equation one can get the generalized gamma function as given in equation (1). On the one hand this new function present a generalization of gamma functions and on the other it proved fundamental to get the new series representation of the λ-generalized Hurwitz-Lerch zeta functions. It is interesting to study the properties of this function that are proved in the form of theorems.

Theorem 1. λ-generalized gamma functions satisfy the following recurrence relation

$$\Gamma_{a,b}^\lambda(s+1) = \frac{s}{a}\Gamma_{a,b}^\lambda(s) + \frac{b\lambda}{a}\Gamma_{a,b}^\lambda(s-\lambda);$$
$$(\Re(a,b) > 0; b = 0; \Re(s) > 0) \quad (9)$$

Proof. Consider the Mellin transform representation (8) for the λ-generalized gamma functions and write
$$\Gamma_{a,b}^\lambda(s) = \mathcal{M}\left[\exp\left(-at - \frac{b}{t^\lambda}\right); s\right]. \quad (10)$$

By taking derivative of the involved function one can get

$$\frac{d}{dt}\left[\exp\left(-at - \frac{b}{t^\lambda}\right)\right]$$
$$= -a \exp\left(-at - \frac{b}{t^\lambda}\right) + b\lambda \frac{\exp\left(-at - \frac{b}{t^\lambda}\right)}{t^{\lambda+1}}$$
$$= \exp\left(-at - \frac{b}{t^\lambda}\right)\left[-a + \frac{b\lambda}{t^{\lambda+1}}\right]. \quad (11)$$

Next, by applying Mellin transform on both sides of (11) and using derivative property of familiar Mellin transform given by, see [50, Chapter 10]

$$\mathcal{M}[g'(t); s] = -(s-1)\mathcal{M}[g(t); s-1] \quad (12)$$

in (11), one can get the required result as stated in equation (9).

Corollary 1. The generalized gamma functions have the following representation

$$\Gamma_b(s+1) = s\Gamma_b(s) + b\Gamma_b(s-1);$$
$$(b > 0; b = 0; \Re(s) > 0) \quad (13)$$

Proof. This holds by simply replacing $a = \lambda = 1$ in equation (9).

Remark 1. Note that for $b = 0$, one can get the functional equation for the original gamma functions such as $\Gamma(s+1) = s\Gamma(s)$.

Theorem 2. Let $1 < p < \infty$ and $\frac{1}{p} + \frac{1}{q} = 1$, then *log-convex property* for the λ-generalized gamma functions is given by

$$\Gamma_{a,b}^\lambda\left(\frac{s}{p} + \frac{u}{q}\right) \leq \left(\Gamma_{a,b}^\lambda(s)\right)^{\frac{1}{p}}\left(\Gamma_{a,b}^\lambda(u)\right)^{\frac{1}{q}} \quad (14)$$

Proof. By making a replacement $s \to \frac{s}{p} + \frac{u}{q}$ in (8), one can get

$$\Gamma_{a,b}^\lambda\left(\frac{s}{p} + \frac{u}{q}\right) = \int_0^\infty t^{\frac{s}{p}+\frac{u}{q}-1} \exp\left(-at - \frac{b}{t^\lambda}\right) dt$$
$$= \int_0^\infty t^{s-1}\exp\left(-at - \frac{b}{t^\lambda}\right)^{\frac{1}{p}} t^{u-1}\exp\left(-at - \frac{b}{t^\lambda}\right)^{\frac{1}{q}} dt \quad (15)$$

Now, by making use of Holder inequality [1], one can get

$$\Gamma_{a,b}^\lambda\left(\frac{s}{p} + \frac{u}{q}\right) \leq \left(\Gamma_{a,b}^\lambda(s)\right)^{\frac{1}{p}}\left(\Gamma_{a,b}^\lambda(u)\right)^{\frac{1}{q}} \text{ which is}$$

exactly (14).

Corollary 2. Prove that the following inequality holds for $s, u > 0; b \geq 0$,

$$\Gamma_{a,b}^{\lambda}\left(\frac{s}{2}+\frac{u}{2}\right) \leq \sqrt{\left(\Gamma_{a,b}^{\lambda}(s)\right)\left(\Gamma_{a,b}^{\lambda}(u)\right)} \qquad (16)$$

Proof. For $\lambda > 0$, setting $p = 2 = q$ in (15), one can obtain the required result (16).

Remark 2. Nevertheless, as the geometric mean of two positive numbers is less than or equal to their arithmetic mean, one can get

$$\Gamma_{a,b}^{\lambda}\left(\frac{s}{2}+\frac{u}{2}\right) \leq \sqrt{\left(\Gamma_{a,b}^{\lambda}(s)\right)\left(\Gamma_{a,b}^{\lambda}(u)\right)}$$
$$\leq \frac{\Gamma_{a,b}^{\lambda}(s) + \Gamma_{a,b}^{\lambda}(u)}{2}, \qquad (17)$$

where, $s, u > 0; b \geq 0$. □

Theorem 3. Prove that the following reflection formula holds true

$$\Gamma_{a,b}^{\lambda}(s) = \lambda b^{s} \Gamma_{1,ab}^{\lambda}(-\lambda s), \Re(b) > 0. \qquad (18)$$

Proof. For $\lambda > 0$, substituting $t = b\tau^{-\lambda}$ and $dt = -b\lambda\tau^{-\lambda-1}$ in (8), one can write as

$$\Gamma_{a,b}^{\lambda}(s) = \int_{0}^{\infty}\left(\frac{b}{\tau^{\lambda}}\right)^{s-1}\exp\left(-a\frac{b}{\tau^{\lambda}}-t\right)(-b\lambda\tau^{-\lambda-1})d\tau$$

$$= \lambda b^{s}\int_{0}^{\infty}\tau^{-\lambda s-1}\exp\left(-\frac{ab}{\tau^{\lambda}}-\tau\right)d\tau, \qquad (19)$$

which is the same result as the requirement of theorem.

Corollary 3. Prove that the following result holds true for generalized gamma function

$$\Gamma_{b}(s) = b^{s}\Gamma_{b}(-s); (\Re(b) > 0; b = 0, \Re(s) > 0) \quad (20)$$

Proof. By replacing $\lambda = a = 1$ in (18), the required result is obtained.

Theorem 4. Prove that the λ-generalized gamma functions have the following derivative

$$\frac{d}{ds}\left(\ln\left(\Gamma_{a,b}^{\lambda}(s)\right)\right) = \frac{\frac{d}{ds}\left(\Gamma_{a,b}^{\lambda}(s)\right)}{\Gamma_{a,b}^{\lambda}(s)},$$
$$(\Re(b) > 0; b = 0, \Re(s) > 0). \qquad (21)$$

Proof. Consider the LHS and differentiate with respect to s to get

$$\frac{d}{ds}\left(\ln\left(\Gamma_{a,b}^{\lambda}(s)\right)\right) = \frac{1}{\Gamma_{a,b}^{\lambda}(s)}\int_{0}^{\infty}\exp\left(-at-\frac{b}{t^{\lambda}}\right)t^{s-1}\ln t\, dt$$
$$= \frac{\frac{d}{ds}\left(\Gamma_{a,b}^{\lambda}(s)\right)}{\Gamma_{a,b}^{\lambda}(s)} \qquad (22)$$

that leads to the required result.

Corollary 4. Prove that the generalized gamma function has derivative [1, p. 23]

$$\psi_{b}(s) = \frac{d}{ds}\left(\ln(\Gamma_{b}(s))\right) = \frac{\frac{d}{ds}(\Gamma_{b}(s))}{\Gamma_{b}(s)},$$
$$\Re(b) > 0; b = 0, \Re(s) > 0) \qquad (23)$$

Proof. By making a replacement $\lambda = a = 1$ in (21), the required result is obtained.

Corollary 5. Prove that the gamma function has derivative [1, p. 20]

$$\psi(s) = \frac{d}{ds}\left(\ln(\Gamma(s))\right) = \frac{\frac{d}{ds}(\Gamma(s))}{\Gamma(s)} \qquad (24)$$

Proof. This holds simply by putting $b = 0$ in (23)

Remark 3. Next, a new series representation for Srivastava's λ-generalized Hurwitz-Lerch zeta functions is obtained by using these newly defined λ-generalized gamma functions. Several special and interesting cases are also obtained.

Theorem 5. Prove that Srivastava's λ-generalized Hurwitz-Lerch zeta functions have the following series representation

$$\Phi_{\lambda_{1},...,\lambda_{p},\mu_{1},...,\mu_{q}}^{(\rho_{1},...,\rho_{p},\sigma_{1},...,\sigma_{q})}(z, s, a; b, \lambda)$$
$$:= \frac{1}{\lambda\Gamma(s)}\sum_{\chi=0}^{\infty}\frac{([\lambda_{p}])_{\rho_{p}\chi}}{([\mu_{q}])_{\sigma_{q}\chi}}\frac{z^{\chi}}{\chi!}\frac{\Gamma_{1,(a+\chi)b}^{\lambda}(s)}{(\chi+a)^{s}} \qquad (25)$$

$$\begin{pmatrix} \lambda i \in \mathbb{R}(i=1,..,p) \text{and } \mu_i \in \mathbb{R}\backslash \mathbb{Z}-\{0\}\ (i=1,...,q); \\ \rho i > 0; \sigma i > 0; 1+\Delta \geq 0 \end{pmatrix}$$

Proof. Consider the integral representation (8)

$$\Phi_{\lambda_1,...,\lambda_p,\mu_1,...,\mu_q}^{(\rho_1,...,\rho_p,\sigma_1,...,\sigma_q)}(z,s,a;b,\lambda):=$$

$$\frac{1}{\Gamma(s)}\int_0^\infty t^{s-1} \exp\left(-at-\frac{b}{t^\lambda}\right) {}_p\Psi_q^*\begin{bmatrix}(\lambda_1,\rho_1),..., & (\lambda_p,\rho_p) \\ (\mu_1,\sigma_1),..., & (\mu_p,\sigma_p)\end{bmatrix};ze^{-t}\Bigg] dt$$

$$(\lambda \geqq 0; \Re(b) \geqq 0; \min[\Re(s),\Re(a)] > 0) \qquad (26)$$

Now replace the normalized fox-wright function by its series representation given by (6) to get

$$\Phi_{\lambda_1,...,\lambda_p,\mu_1,...,\mu_q}^{(\rho_1,...,\rho_p,\sigma_1,...,\sigma_q)}(z,s,a;b,\lambda)$$

$$:=\frac{1}{\Gamma(s)}\sum_{\chi=0}^\infty \frac{([\lambda_p])_{\rho_p\chi}}{([\mu_q])_{\sigma_q\chi}}\frac{z^\chi}{\chi!}\int_0^\infty t^{s-1}\exp\left(-(a+\chi)t-\frac{b}{t^\lambda}\right)dt \quad (27)$$

Order of summation and integration is interchangeable due to uniform convergence of the integral. Next by replacing $(a+\chi)t \rightarrow \tau$ in the above equation (27) and then using the definition of λ-generalized gamma functions (8), the required result is obtained.

Remark 4. Such conclusions corresponding to further associated functions as enumerated in Table 1, in view of altered parameter values in the form of series representations can be obtained. For example, Fermi-Dirac and Bose-Einstein functions are of fundamental importance in Quantum Statistics and related sciences [22, 33-36]. By considering row 3 of Table 1 and this new representation (25), one can get a new series representation for these functions but also for their more general forms such as

$$F_{\lambda_1,...,\lambda_p,\mu_1,...,\mu_q}^{(\rho_1,...,\rho_p,\sigma_1,...,\sigma_q)}(x,s;b,\lambda)$$

$$:=\frac{1}{\lambda\Gamma(s)}\sum_{\chi=0}^\infty \frac{([\lambda_p])_{\rho_p\chi}}{([\mu_q])_{\sigma_q\chi}}\frac{(-e^{-x})^\chi}{\chi!}\frac{\Gamma_{1,(a+\chi)b}^\lambda(s)}{(\chi+a)^s}; \quad (28)$$

$$B_{\lambda_1,...,\lambda_p,\mu_1,...,\mu_q}^{(\rho_1,...,\rho_p,\sigma_1,...,\sigma_q)}(x,s;b,\lambda)$$

$$=\frac{1}{\lambda\Gamma(s)}\sum_{\chi=0}^\infty \frac{([\lambda_p])_{\rho_p\chi}}{([\mu_q])_{\sigma_q\chi}}\frac{(e^{-x})^\chi}{\chi!}\frac{\Gamma_{1,(a+\chi)b}^\lambda(s)}{(\chi+a)^s}. \quad (29)$$

These representations (28) and (29) are achieved from (25) by using $z=\pm e^{-x}$.

By considering $p-1=q=0\ (\lambda_1=\mu; \rho_1=1)$, $b\neq 0$, in equation (28) and (29) one can get the following from

$$F_\mu^\lambda(x,s;b) = \frac{1}{\Gamma(s)}\sum_{\chi=0}^\infty \frac{(\mu)_\chi(-e^{-x})^\chi \Gamma_{1,(a+\chi)b}^\lambda(s)}{\chi!(\chi+a)^s}; \quad (30)$$

$$B_\mu^\lambda(x,s;b) = \frac{1}{\Gamma(s)}\sum_{\chi=0}^\infty \frac{(\mu)_\chi(e^{-x})^\chi \Gamma_{1,(a+\chi)b}^\lambda(s)}{\chi!(\chi+a)^s}. \quad (31)$$

By considering other parametric values as, $p-1=q=0\ (\lambda_1=\mu; \rho_1=1)$, $b\neq 0; \lambda=\mu=1$ the above result (25) shrink instantly to the subsequent results:

$$\Phi_b(s,z,a) = \frac{1}{\Gamma(s)}\sum_{\chi=0}^\infty \Gamma_{(a+\chi)b}(s)(z)^\chi(\chi+a)^{-s}; \quad (32)$$

$z=1$

$$\zeta_b(s,a) = \frac{1}{\Gamma(s)}\sum_{\chi=0}^\infty \Gamma_{(a+\chi)b}(s)(\chi+a)^{-s}; \quad (33)$$

$a=1$

$$\zeta_b(s) = \frac{1}{\Gamma(s)}\sum_{\chi=0}^\infty \Gamma_{(a+\chi)b}(s)(\chi+1)^{-s}. \quad (34)$$

Taking $p-1=q=0\ (\lambda_1=\mu; \rho_1=1)$, $b=0$, in the main result (25), the following series representations are obtained

$$\Phi_\mu^*(s,z,a) = \frac{1}{\Gamma(s)}\sum_{\chi=0}^\infty \frac{(z)^\chi(\mu)_n}{n!(\chi+a)^s}, \quad (35)$$

taking $z=1$

$$\zeta_\mu^*(s,a) = \sum_{\chi=0}^\infty \frac{(\mu)_n}{n!(\chi+a)^s}, \quad (36)$$

further, $a=1$

$$\zeta_\mu^*(s) = \sum_{\chi=0}^\infty \frac{(\mu)_n}{n!(\chi+1)^s}. \quad (37)$$

Next by putting $b = 0$ in the above equations (32)-(34), we get the following known and widely studied representations that can be found in any of the references [1-50]

$$\Phi(s, z, a) = \sum_{\chi=0}^{\infty} \frac{(z)^{\chi}}{(\chi + a)^s}; \qquad (38)$$

$z = 1$

$$\zeta(s, a) = \sum_{\chi=0}^{\infty} \frac{1}{(\chi + a)^s}; \qquad (39)$$

$a = 1$

$$\zeta(s) = \sum_{\chi=0}^{\infty} \frac{1}{(\chi + 1)^s}. \qquad (40)$$

Remark 2: Note that the coefficients in the above series represenatations equations (38)-(40) are 1, while in equations (35)-(37) these are ratios of gamma functions (namely Pochhammer symbols). In more general cases equations (32)-(34) these coefficients are generalized gamma functions while for our main result (25) and (26)-(28), these are the λ-generalized gamma functions. To confirm the consistency of the results obtained by new representation, it can be noted that the new result (25) generates (38)-(40) as special cases that are well known results in Analytic Number Theory.

3. Conclusion

In this article, a new generalization of gamma functions is introduced. Some properties of these newly defined family of the λ-generalized gamma functions are discussed that is a fundamental aspect of the analysis of special functions. As an application of these new functions, a new series representation for λ-generalized Hurwitz-Lerch zeta functions is derived that proved worthwhile to provide significant new results in this investigation. The known results can be obtained as distinct cases of these new results.

3.1. Comparison with existing methods

Usually a function is defined in the form of an integral or a series of some variables, or in terms of basic functions. Though, it requires to be considered as an element by itself, categorized by an integral or a series. Then it can be studied beyond its unique domain of explanation and can be used in diverse situations. This apprehension comes to be more substantial for the analysis of special functions. This type of functions are expressed in wide domains by using series, asymptotic, and integral representations. This fact is also important to write more simple mathematical proofs. Consequently, a new representation for Srivastava's λ-generalized Hurwitz-Lerch zeta functions has been obtained. It yields similar representation for all members of the family of zeta functions. Several authors studied these functions, but no work has been reported for their presentation in relation with generalized gamma functions. These are some straightforward examples, it is expected that some more identities can be obtained by using these new functions and their representations.

Conflict of Interest

None declared

Acknowledgements

References

Chaudhry, M. A.; Zubair, S.M., On a Class of Incomplete Gamma Functions with Applications, Chapman and Hall (CRC Press Company), Boca Raton, London, New York and Washington, D.C., (2001).

Srivastava, H.M, A new family of the λ-generalized Hurwitz-Lerch Zeta functions with applications, Appl. Math. Inf. Sci. 8 (2014) 1485–1500.

Srivastava, H.M.; Jankov, D.; Pogany, T.K.; Saxena, R.K., Integral and computational representations of the extended Hurwitz-Lerch Zeta function, Integral Transforms Spec. Funct., 22, 487–506 (2011]

Srivastava, H.M.; Jankov, D.; Pogany, T.K.; Saxena, R.K., Two-sided inequalities for the extended Hurwitz-Lerch Zeta function, Comput. Math. Appl., 62 (2011) , 516–522 (2011).

Tassaddiq, A. A new representation of the k-gamma functions. Mathematics, 2019, 10, 733.

Kilbas, A.A.; Saigo, M., H-Transforms: Theory and Applications, Chapman and Hall (CRC Press Company), Boca Raton, London, New York and Washington, D.C., (2004).

Mathai, A.M.; Saxena, R.K, The H-Functions with Applications in Statistics and Other Disciplines, Wiley Eastern Limited, New Delhi, (1978).

Mathai, A.M.; Saxena, R.K.; Haubold, H.J., The H-Function: Theory and Applications, Springer, New York, Dordrecht, Heidelberg and London, (2010).

Olver, F.W.J.; Lozier, D.W.; Boisvert, R.F.; Clark, C.W. (Editors), NIST Handbook of Mathematical Functions [With 1 CD-ROM (Windows, Macintosh and UNIX)], U. S. Department of Commerce, National Institute of Standards and Technology, Washington, D. C., (2010); Cambridge University Press, Cambridge, London and New York, (2010)

Luo, M.-J.; Raina, R.K., New Results for Srivastava's λ-Generalized Hurwitz-Lerch Zeta Function, Filomat 31:8 (2017), 2219–2229.

Jankov, D.; Pogany, T.K.; Saxena, R.K., An extended general Hurwitz-Lerch Zeta function as a Mathieu ´ (a, λ)-series, Appl. Math. Lett. 24 (8) (2011) 1473–1476

Srivastava, H.M.; Ghanim, F.; El-Ashwah, R.M., Inclusion properties of certain subclass of univalent meromorphic functions defined by a linear operator associated with the λ-generalized Hurwitz-Lerch zeta function, BULETINUL ACADEMIEI DE S¸TIINT¸E A REPUBLICII MOLDOVA. MATEMATICA, 3(85), 2017, Pages 34–50

Srivastava, H.M., Gaboury, S., New expansion formulas for a family of the λ-generalized Hurwitz-Lerch zeta functions, Internat. J. Math. Math. Sci., 2014, 2014, Article ID 131067, 1–13.

Srivastava, H.M.; Gaboury, S.; Ghanim, F., Certain subclasses of meromorphically univalent functions defined by a linear operator associated with the λ-generalized Hurwitz-Lerch zeta function, Integral Transforms Spec. Funct.,26 (2015), 26, 258–272.

H. M. Srivastava, S. Gaboury, F. Ghanim, Some further properties of a linear operator associated with the λ-generalized Hurwitz-Lerch zeta function related to the class of meromorphically univalent functions, Appl. Math. Comput., 2015, 259, 1019–1029.

Srivastava, H.M., Some properties and results involving the zeta and associated functions, Functional Analysis, Approximation and Computation, 7 (2) (2015), 89–133

Choi, J.; Parmar, R.K., An Extension of the Generalized Hurwitz-Lerch Zeta Function of Two Variables, Filomat 31:1 (2017), 91–96 DOI 10.2298/FIL1701091C

Srivastava, H.M.; Jolly, N.; Kumar, B.; Manish Jain, R.,A new integral transform associated with the extended Hurwitz–Lerch zeta function. Revista de la Real Academia de Ciencias Exactas, Físicas y Naturales. Series A. Matemáticas. 10.1007/s13398-018-0570-4. . (2018).

Tassaddiq, A., A New Representation for Srivastava's λ-Generalized Hurwitz-Lerch Zeta Functions. Symmetry 2018, 10, 733.

Tassaddiq, A. Some difference equations for

Srivastava's λ-generalized Hurwitz–Lerch zeta functions with applications, Symmetry, 2019, 11, 311

Apostol, T. M. Introduction to Analytic Number Theory, (Springer-Verlag, Berlin, New York and Heidelberg, 1976).

Chaudhry, M.A.; Qadir, A.; Tassaddiq, A. A new generalization of the Riemann zeta function, Adv. Difference Equ. 2011, 2011:20.

Titchmarsh, E. C. The Theory of the Riemann Zeta Function, Oxford University Press, 1951.

Raina, R.K.; Srivastava, H.M., Certain results associated with the generalized Riemann zeta functions, Rev. Tec. Ing. Univ. Zulia, 18 (3) (1995), 301-304.

Srivastava, H.M., Some formulas for the Bernoulli and Euler polynomials at rational arguments, Math. Proc. Cambridge Philos. Soc., 129, 77–84 (2000).

Srivastava, H.M., Generating relations and other results associated with some families of the extended Hurwitz- Lerch Zeta functions, SpringerPlus, 2, Article ID 2:67, 1-14(2013).

Srivastava, H.M.; Choi, J., Series Associated with the Zeta and Related Functions, Kluwer Academic Publishers, Dordrecht, Boston and London, (2001).

Srivastava, H.M.; Choi, J., Zeta and q-Zeta Functions and Associated Series and Integrals, Elsevier Science Publishers, Amsterdam, London and New York, (2012).

Srivastava, H.M.; Gupta, K.C.; Goyal, S.P., The H-Functions of One and Two Variables with Applications, South Asian Publishers, New Delhi and Madras, (1982).

Srivastava, H.M.; Karlsson, P.W., Multiple Gaussian Hypergeometric Series, Halsted Press (Ellis Horwood Limited, Chichester), John Wiley and Sons, New York, Chichester, Brisbane and Toronto, (1985).

Srivastava, H.M.; Manocha, H.L, A Treatise on Generating Functions, Halsted Press (Ellis Horwood Limited, Chichester), John Wiley and Sons, New York Chichester, Brisbane and Toronto, (1984).

Srivastava, H.M., Some generalizations and basic (or q-) extensions of the Bernoulli, Euler and Genocchipolynomials, Appl. Math. Inform. Sci., 5, 390–444 (2011).

Tassaddiq, A., Some Representations of the Extended Fermi-Dirac and BoseEinstein Functions with Applications. Ph.D. Dissertation, National University of Sciences and Technology Islamabad, Pakistan, (2011).

Tassaddiq, A.; Qadir, A., Fourier transform representation of the extended Fermi-Dirac and Bose-Einstein functions with applications to the family of the zeta and related functions, Integral Transforms Spec. Funct,, 22 (6) (2011), 453-466.

A. Tassaddiq and A. Qadir, Fourier transform and distributional representation of the generalized gamma function with some applications, Appl Math. Comput. 218 (2011), 1084-1088.

A. Tassaddiq, A New Representation of the Extended Fermi-Dirac and Bose-Einstein Functions, International Journal of Mathematics and its Applications, 5 (2) (2017), 435-446.

Gaboury, S.; Bayad, A, Series representations at special values of generalized Hurwitz-Lerch zeta function, Abstr. Appl. Anal., 2013, Article ID 975615, 1–8 (2013).

Garg, M.; Jain, K.; Kalla, S.L. A further study of general Hurwitz-Lerch zeta function, Algebras Groups Geom., 25 (2008), 311–319 (2008)

Garg, M.; Jain, K.; Srivastava, H.M., Some relationships between the generalized Apostol-Bernoulli polynomials and Hurwitz-Lerch Zeta functions, Integral Transforms Spec. Funct., 17 (2006), 803–815.

Gupta, P.L.; Gupta, R.C.; Ong, S.-H.; Srivastava, H.M., A class of Hurwitz-Lerch Zeta distributions and their applications in reliability, Appl. Math. Comput., 196, 521–531 (2008).

Lin, S.-D.; Srivastava, H.M., Some families of the Hurwitz-Lerch Zeta functions and associated fractional derivative and other integral representations, Appl. Math. Comput., 154, 725–733 (2004).

Lin, S.-D.; Srivastava, H.M.; Wang, P.-Y., Some expansion formulas for a class of generalized Hurwitz-Lerch Zeta functions, Integral Transforms Spec. Funct., 17, 817–827 (2006).

Lippert, R. A. A probabilistic interpretation of the Hurwitz zeta function, Adv. Math., 97, 278–284 (1993).

Saxena, R.K.; Pogany, T.K.; Saxena, R.; Jankov, D., On generalized Hurwitz-Lerch Zeta distributions occurring in statistical inference, Acta Univ. Sapientiae Math., 3, 43–59 (2011).

Raina, R.K.; Chhajed, P.K., Certain results involving a class of functions associated with the Hurwitz zeta function, Acta Math. Univ. Comenianae, 73, 89–100 (2004).

Srivastava, H.M.; Luo, M.-J.; Raina, R.K., New results involving a class of generalized Hurwitz-Lerch zeta functions and their applications, Turkish J. Anal. Number Theory, 1, 26-35 (2013).

Erdelyi, A.; Magnus, W.; Oberhettinger, F.; Tricomi, F.G. Higher Transcendental Functions,, McGraw-Hill Book Company, New York, Toronto and London, I, (1953).

Bayad, A.; Chikhi, J., Reduction and duality of the generalized Hurwitz-Lerch zetas, Fixed Point Theory Appl., 2013, Article ID 82, 1–14 (2013)

Srivastava, H.M.; Chaudhry, M.A.; Qadir, A.; Tassaddiq, Some extensions of the Fermi-Dirac and Bose-Einstein functions with applications to zeta and related functions, Russian J. Math. Phys, 18 (2011), 107-121.

Zayed, A.I. Handbook of Functions and Generalized Function Transforms, CRC Press, Boca Raton, 1996.

Appendix A. Derivation of equation (22)

$$\frac{d}{ds}\left(ln\left(\Gamma_{a,b}^{\lambda}(s)\right)\right) = \frac{1}{\Gamma_{a,b}^{\lambda}(s)}\frac{d}{ds}\int_0^{\infty}exp\left(-at-\frac{b}{t^{\lambda}}\right)t^{s-1}\,dt$$

$$= \frac{1}{\Gamma_{a,b}^{\lambda}(s)}\int_0^{\infty}exp\left(-at-\frac{b}{t^{\lambda}}\right)\frac{d}{ds}t^{s-1}\,dt$$

$$= \frac{1}{\Gamma_{a,b}^{\lambda}(s)}\int_0^{\infty}exp\left(-at-\frac{b}{t^{\lambda}}\right)t^{s-1}lnt\,dt$$

$$= \frac{\frac{d}{ds}\left(\Gamma_{a,b}^{\lambda}(s)\right)}{\Gamma_{a,b}^{\lambda}(s)}\quad (A-1)$$

Journal of Engineering and Applied Sciences (JEAS)